which is only 0.04 eV higher in energy and has $11\mu_B$ magnetic moments. This will be also abundant in experimental conditions and will give rise to an average lower magnetic moment on this cluster and therefore a better agreement with the experimental[1] value of $0.48\pm0.13\mu_B$/atom. This is in contrast to the value of $1.62\mu_B$/atom obtained by Reddy *et al.*[5] using the local density functional theory while Jinlong *et al.* as well as Reddy *et al.*[6] obtained $1.15\mu_B$/atom for this cluster. As we shall show later, there is some directionality in bonding in isomer (13b). This is also seen from the fact that a nearly hexagonal prism isomer with an atom at the center lies 0.44 eV higher in energy with $15\mu_B$ magnetic moment than isomer (13b). The latter is important as Rh_{14} is obtained from it. We also show two more isomers (13c and 13d) that are 0.08 eV [with $15\mu_B$ magnetic moments and somewhat similar to (13a)] and 0.17 eV (decahedral with $17\mu_B$ magnetic moment) higher in energy than the isomer (13a). Many other isomers were also studied but these are higher in energy.

A few optimized structures for Rh_{14} are shown in Fig. 2. The lowest energy isomer of Rh_{14} is obtained from isomer (13b) by capping a hexagonal face. It has $16\mu_B$ magnetic moments. A hexagonal anti-prism with each hexagon having an atom at the center (14b) is nearly degenerate with $16\mu_B$ magnetic moments. In this case there is no atom at the center. Another isomer with three-fold symmetry and no atom at the center (14c) lies 0.52 eV higher in energy with $18\mu_B$ magnetic moments. A capped icosahedron (14d) lies 0.62 eV higher in energy, again showing that icosahedral growth is not favored. A cubic isomer with capping of the six faces lies 0.52 eV higher in energy and has $18\mu_B$ magnetic moments. The lowest energy structure of Rh_{15} is derived from the lowest energy isomer of Rh_{13}. It has an atom at the center of a bent hexagon with a tetramer on either side and $19\mu_B$ magnetic moments. There are several other isomers that have lower or equal magnetic moments and which will be present in experiments below room temperature and give rise to a lower estimation of the magnetic moments on this cluster. Two such isomers are shown in Fig. 2. The isomer (15b) is derived from (14a) with both hexagonal (the six atoms are not in a plane) faces capped while (15c) has two layers with no atom at the center. These results show that relatively open (noncompact structures) are more favored by Rh clusters. Some of the properties of the lowest energy isomers of $n=13-15$ clusters are given in Table I.

In general we find an abundance of rhombii in the lowest energy structures of Rh clusters. Starting from Rh_4, one can consider the growth process to follow from addition of an atom to an existing cluster with significant relaxations. This way one can account for the growth upto $n=10$. Rh_{11} can be considered to be a symmetrical capping by two atoms on a Rh_9 cluster having a capped tetragonal antiprism structure. However, the capped tetragonal antiprism isomer of Rh_9 lies significantly higher in energy. So the growth process can be quite complex and in the cases where more than one isomer are nearly degenerate, there could be different routes for the growth of these clusters.

B. Cagelike structure

The result that icosahedron is not of the lowest energy for Rh_{13} and that a relatively open cage structure has lower energy is significant in understanding the growth behavior of transition metal clusters. In fact non-icosahedral growth was also reported earlier[12] for Nb clusters. In order to check if a similar behavior would be found in clusters of Pd and Ru that are neighboring elements to Rh in the periodic table, we performed calculations for Pd_{13} and Ru_{13}. It is found that in these cases also an icosahedron is not of the lowest energy. For Ru_{13} the second best isomer (13b) of Rh_{13} has the lowest energy with $4\mu_B$ magnetic moments while the one with the structure of the best isomer (13a) of Rh_{13} lies 1.56 eV higher in energy with $2\mu_B$ magnetic moments. Changing the spin in these isomers costs little energy (see Fig. 3 for Rh clusters) and therefore the magnetic moments can be easily supressed in these clusters. The icosahedral isomer lies 2.25 eV higher in energy and has a large magnetic moment of $12\mu_B$. Therefore icosahedral structure is very unfavorable for Ru and our results explain the nearly nonmagnetic behavior found in these clusters in experiments.[1] For Pd_{13} the best structure of Rh_{13} also has the lowest energy with $8\mu_B$ magnetic moments but an icosahedral isomer reported earlier[3] lies only 0.05 eV higher in energy with $8\mu_B$ magnetic moment. Therefore for Pd_{13} these two isomers are nearly degenerate. The bonding in

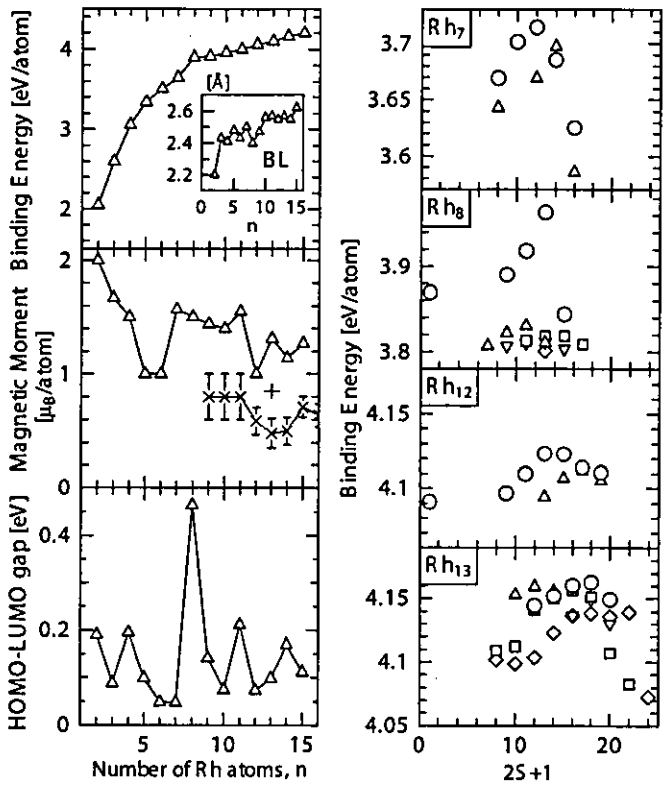

FIG. 3. Binding energies, magnetic moments, and HOMO-LUMO gaps of Rh_n clusters are plotted in the left panel. A plus (+) shows the magnetic moment of the isomer (13b) which gives a much better agreement with the overall trend found in experimental results which are shown by crosses with error bars. Inset shows the mean nearest neighbor bond lengths. The energies of the spin isomers are shown for $n=7$, 8, 12, and 13 in the right panel. S equals half the value of the total magnetic moment. Circles, triangles, squares, reverse triangles, and diamonds represent, respectively, the isomers (a)–(e) in Figs. 1 and 2.

Pd clusters is much weaker as delocalization of $4d$ electrons occurs slowly and this could explain why icosahedral structure becomes more favorable in Pd. The lowest energy isomer of Ru_{13} [(13b) in Fig. 2] lies 0.81 eV higher in energy for Pd and has $6\mu_B$ magnetic moments. Therefore, the behaviors of Pd and Ru clusters are quite different. A decahedron of Pd_{13} lies 0.34 eV higher in energy and has $8\mu_B$ magnetic moments. These results show that Pd_{13} has the same magnetic moments in quite different structures.

C. Calculated properties

The BE is shown in Fig. 3 for the lowest energy isomers of Rh clusters. It increases monotonically as the cluster size increases and has a small peak at $n=8$. Interestingly there is also a significant highest occupied-lowest unoccupied molecular orbital (HOMO-LUMO) gap for Rh_8 making it behave like a magic cluster. In most of the other clusters the HOMO-LUMO gap is generally small and shows an oscillatory behavior. There is an overall decrease with an increase in size. This is expected as bulk Rh is a metal. The magnetic moments per Rh atom (Fig. 3) show an oscillatory behavior as a function of the cluster size but overall there is a decreasing trend as the bulk is nonmagnetic. The magnetic moment is nearly constant in the range of $n=7-11$ and for $n=12$ there is a significant drop. These results agree well with the experimental data[1] that show $0.8\pm0.2\mu_B$/atom magnetic moment for $n=9-11$ and then $0.59\pm0.12\mu_B$/atom for $n=12$. Also our result of $0.85\mu_B$/atom magnetic moment for the isomer (13b) agrees well with an experimental decrease in the magnetic moment from $n=12$ to 13 and then for $n=14$ and 15, there is an increase in the magnetic moment again in agreement with the trend found in experiments (experimetal values being 0.50 ± 0.12 and $0.71\pm0.09\mu_B$/atom for $n=14$ and 15, respectively). The overall good agreement with the experimetal results gives us confidence that our calculated lowest energy structures are close to the experimental findings. The experimetal values of the magnetic moments are nearly uniformly lower and this could be due to the fact that theoretical results are at zero temperature while experimental results correspond to temperatures in the range of 60–300 K. We have also shown the variation in the energy of the spin isomers considering the cases of clusters with $n=7$, 8, 12, and 13. This is generally small as the total spin is changed to a lower value while the energy decreases more sharply for higher spin isomers. As mentioned before, this could account for the observed lower magnetic moments because isomers with lower magnetic moments would also be present. Our finding of a new isomer of $n=13$ is particularly noteworthy and this could explain the much lower magnetic moments observed for Rh_{13}.

It is worth to point out here that in our studies we have ignored orbital contribution to the magnetic moments. In recent years there are efforts[17] to include the orbital contribution as well as the magnetic anisotropy in clusters. The orbital contribution would increase the total magnetic moment and therefore would lead to a larger difference with the experimental results. Guirado-Lopez *et al.*[18] have calculated the orbital magnetic moments for Rh clusters using a self-consistent tight-binding method and representative face center cubic structures with bulk nearest neighbor bond lengths. The average orbital magnetic moments have been reported to lie in the range of $0.1-0.24\mu_B$/atom for $n\leq19$ with strong oscillations as a function of n. The orbital contribution to the magnetic moments is expected to be sensitive to the structures of clusters and as our results show, the structures of Rh clusters are generally very different from the high symmetry structures considered by these authors. We shall expect that the significantly lower symmetry in most cases of Rh clusters would lead to a reduced contribution from orbital magnetic moments. Further, in order to find a correlation between the magnetic moments and the bond lengths or the coordination number, we calculated the local magnetic moments around each ion for a few clusters. However, we do not find a systematic trend. In general a higher coordination or a short bond length reduces magnetic moments due to the increased hybridization. This can be seen from the lowest energy isomer of Rh_6. In this isomer there is one bond which is shortest (2.36 Å) and the local magnetic moments on the two atoms are the smallest ($\approx0.8\mu_B$) while on the remaining atoms the magnetic moments are $\approx1.1\mu_B$. In this case the coordination of each atom is 3 and therefore the short bond is responsible for the reduced moment. However, in the case of the lowest energy isomer of Rh_{13}, an atom with coordination 7 has magnetic moments of $0.97\mu_B$, whereas the other two atoms with coordination 7 have 1.45 and $1.17\mu_B$ magnetic moments. Therefore, there does not appear to be a straightforward correlation with the coordination number. Similarly in the case of the lowest energy isomer of Rh_{11}, most of the atoms have coordination 5 and two atoms have coordination 4 while one atom has coordination 6. In this case the local magnetic moments have values lying in between 1.22 and $1.59\mu_B$. Atoms with coordination 4 are symmetrically located and have $1.22\mu_B$ magnetic moments while two symmetrically placed atoms with coordination 5 have the highest local magnetic moments of $1.59\mu_B$. An atom with coordination 6 has the local magnetic moments of $1.44\mu_B$. Further calculations on Rh_{14} show that an atom with coordination 3 has the highest magnetic moment of $1.39\mu_B$. For this atom the nearest neighbor bond lengths have values of about 2.61, 2.61, and 2.65 Å while a few other atoms with coordination ranging from 3 to 5 have reduced local magnetic moments of about $1.02\mu_B$ due to the short nearest neighbor bonds of about 2.44 Å. The atom with the highest coordination of 8 has the local magnetic moment of $1.08\mu_B$. We also studied the local moments in the case of the lowest energy isomer of Rh_{15}. Two symmetrically placed atoms with coordination 6 have the lowest local magnetic moments of $0.98\mu_B$ while the atom at the center with coordination 8 has the local magnetic moments of $1.05\mu_B$. On other atoms the local magnetic moments lie in the range of $1.23-1.41\mu_B$ though the coordination changes from 3 to 5. These results show the complex nature of the magnetic moments in these clusters, though in all cases we obtain ferromagnetic coupling.

The calculated mean bond lengths for Rh clusters are shown in the inset of Fig. 3 and the values are also given in Table I. For small clusters there is significant contraction and the bond length approaches towards the calculated bulk value (2.71 Å) in an oscillatory manner. Rh_8 has short bond

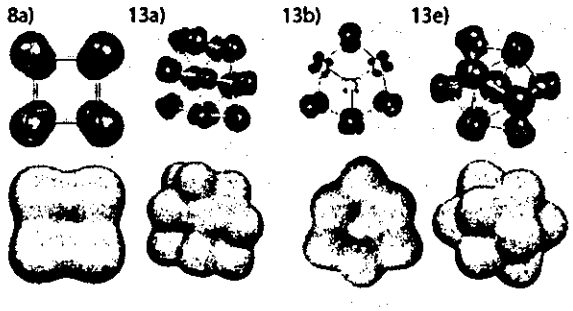

FIG. 4. (Color online) Spin-polarization (upper) and isosurfaces (lower) of the total charge density for isomers (8a), (13a), (13b), and (13e).

lengths which have the lowest value after $n=2$. Also in some clusters such as isomer (13b), there are many short bonds [bond lengths 2.39, 2.41, 2.44, 2.46 Å as compared to the mean bond length of 2.57 Å in isomer (13a)] which indicate directional bonding and covalent character in these clusters. We also calculated the mean coordination in these clusters and for the lowest energy isomers of Rh_n with $n=4-15$, the values are 2, 3.2, 3, 3.71, 3, 3.56, 4.8, 4.91, 4.67, 4.92, 4.14, and 4.67. Some clusters have low mean coordination such as $n=8$ and 14. Also the second lowest energy isomer of $n=13$ has the mean coordination of 3.69. These reflect covalent character of bonding in these clusters. It is more clearly seen from the isosurfaces of the magnetic polarization and the charge densities shown in Fig. 4 for a few selected isomers of Rh_{13} and the lowest energy isomer of Rh_8. In the case of isomers (13a) and (13e) the polarization is nearly uniformly distributed over the whole cluster, while in the case of the isomer (13b) the central atom and four atoms at the surface of the cluster have much less polarization than the rest of the atoms. These atoms have higher coordination. The bond lengths are short (2.51 Å) with four symmetic atoms and 2.58 Å with two atoms from the center) but not the shortest. The central atom has the highest coordination and the lowest polarization. So a higher coordination reduces the magnetic moments significantly but short bond lengths are also responsible for much reduced magnetic moments in this cluster. This leads to much more hybridization between the *sp-d* states which is also seen from the plots of the angular momentum decomposed density of states (Fig. 5). Also for the isomers (13a) and (13e) the charge densities are more uniformly distributed [though isomer (13a) appears to have some covalent character] while for isomer (13b), the covalent character is quite clear. In Rh_8 the charge density and polarization are symmetric reflecting the underlying symmetry of the cluster, but the directional bonding does not appear to be very strong. These results are important revelations of the nature of bonding and unexpected relatively open structures in clusters of these transition metals. The angular momentum decomposed and gaussian broadened densities of states show (Fig. 5) that the *sp-d* hybridization in the case of the isomer (13b) is more significant than in isomer (13a). Also the HOMO lies in a large gap in the up-spin states of the isomer (13a) though the other states are generally uniformly distributed due to the low symmetry of this cluster. On the other hand for the isomer (13b) the HOMO lies in a very small gap and there are many unoccupied states in the up-spin energy spectrum.

IV. SUMMARY

We have studied from first principles the atomic and electronic structures of small Rh clusters and found for the first time relatively open structures to be lower in energy than the icosahedral structures obtained before. In general these isomers have lower magnetic moments and this result is in better agreement with the available experimental data. In particular clusters with 13 or less number of atoms have no atom at the center. Though an atom goes at the center for clusters having more than 13 atoms, the structures are not the closest packed. We find an isomer of 13-atom cluster which is nearly degenerate with the lowest energy isomer and has a

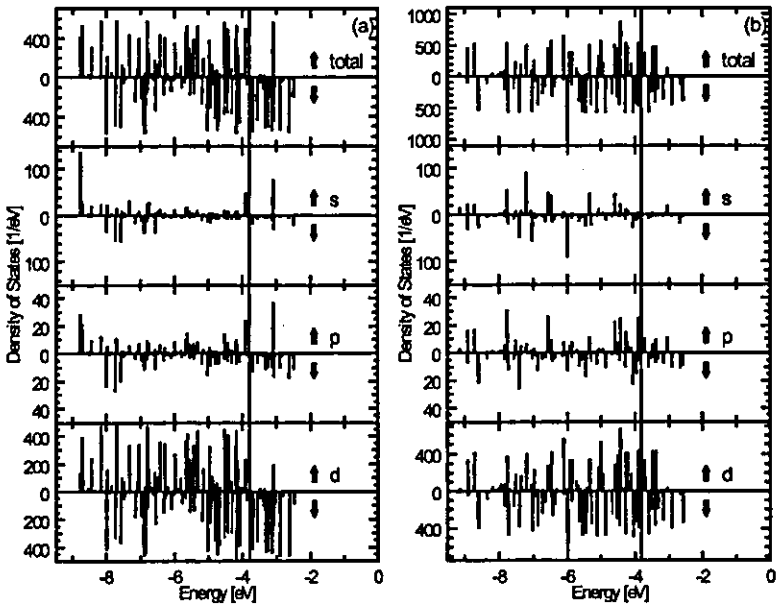

FIG. 5. Gaussian broadened total and angular momentum decomposed electronic states of (13a) and (13b) isomers. The vertical line shows the HOMO.

significantly lower magnetic moment. The latter is in better agreement with the experimental result. In general we find several isomers which lie close in energy and therefore, it is very likely that in experiments one has these isomers unless these are performed at very low temperatures. Our results also show that there is some covalent bonding character in these clusters that is responsible for the relatively open structures. Rh_8 is found to be magic. Further, our preliminary studies on Ru and Pd clusters show that similar structures are lower in energy for Ru clusters than those based on the icosahedral growth while for Pd clusters, the two growth modes may be nearly degenerate. Our results thus open a new chapter in the study of this important class of transition metal clusters. This would lead to a better understanding of the physicochemical properties of these clusters and reactions and to a better design of catalysts.

ACKNOWLEDGMENTS

The authors would like to thank the staff of the Center for Computational Materials Science of the Institute for Materials Research, Tohoku University for their continuous support of the supercomputing facility. V.K. thankfully acknowledges the kind hospitality at the IMR.

[1] A.J. Cox, J.G. Louderback, and L.A. Bloomfield, Phys. Rev. Lett. **71**, 923 (1993); A.J. Cox, J.G. Louderback, S.E. Apseal, and L.A. Bloomfield, Phys. Rev. B **49**, 12 295 (1994).

[2] V. Kumar, K. Esfarjani, and Y. Kawazoe, in *Clusters and Nanomaterials*, edited by Y. Kawazoe, T. Kondow, and K. Ohno, Springer Series in Cluster Physics (Springer-Verlag, Heidelberg, 2002), p. 9.

[3] V. Kumar and Y. Kawazoe, Phys. Rev. B **66**, 144413 (2002).

[4] V. Kumar and Y. Kawazoe, Eur. Phys. J. D **24**, 81 (2003).

[5] B.V. Reddy, S.N. Khanna, and B.I. Dunlap, Phys. Rev. Lett. **70**, 3323 (1993).

[6] B.V. Reddy, S.K. Nayak, S.N. Khanna, B.K. Rao, and P. Jena, Phys. Rev. B **59**, 5214 (1999).

[7] Y. Jinlong, F. Toigo, and W. Kelin, Phys. Rev. B **50**, 7915 (1994).

[8] C. Barreteau, R. Guirado-Lopez, D. Spanjaard, M.C. Desjonqueres, and A.M. Oles, Phys. Rev. B **61**, 7781 (2000); R. Guirado-Lopez, M.C. Desjonqueres, and D. Spanjaard, *ibid.* **62**, 13 188 (2000).

[9] I.M.L. Bilas, A. Chatelian, and W.A. de Heer, Science **265**, 1682 (1994).

[10] O. Eriksson, A. M. Boring, R. C. Albers, G. W. Fernando, and B. R. Cooper, Phys. Rev. B **45**, 2868 (1992); M. Alden, S. Mirbt, H. L. Skriver, N. M. Rosengaard, and B. Johansson, *ibid.* **46**, 6303 (1992).

[11] J. Wei and E. Iglesia, J. Catal. **225**, 116 (2004).

[12] V. Kumar and Y. Kawazoe, Phys. Rev. B **65**, 125403 (2002).

[13] G. Kresse and J. Hafner, J. Phys.: Condens. Matter **6**, 8245 (1994).

[14] G. Kresse and J. Furthmüller, Phys. Rev. B **54**, 11 169 (1996); Comput. Mater. Sci. **6**, 15 (1996).

[15] J.P. Perdew, in *Electronic Structure of Solids*, edited by P. Ziesche and H. Eschrig (Akademie Verlag, Berlin, 1991).

[16] K.A. Gingerich and D.L. Cocke, J. Chem. Soc., Chem. Commun. **1**, 536 (1972).

[17] R. A. Guirado-Lopez, J. Dorantes-Davila, and G. M. Pastor, Phys. Rev. Lett. **90**, 226402 (2003); A. N. Andriotis and M. Menon, *ibid.* **93**, 026402 (2004); J.T. Lau, A. Föhlisch, R. Nietubyc, M. Reif, and W. Wurth, *ibid.* **89**, 057201 (2002); X. Wan, L. Zhou, J. Dong, T.K. Lee, and D.-S. Wang, Phys. Rev. B **69**, 174414 (2004).

[18] R. Guirado-Lopez, P. Villasenor-Gonzalez, J. Dorantes-Davila, and G.M. Pastor, Eur. Phys. J. D **24**, 73 (2003).

NANO LETTERS

2004
Vol. 4, No. 4
677–681

Smallest Magic Caged Clusters of Si, Ge, Sn, and Pb by Encapsulation of Transition Metal Atom

Vijay Kumar,*,†,‡ Abhishek Kumar Singh,† and Yoshiyuki Kawazoe†

Institute for Materials Research, Tohoku University, Sendai 980-8578, Japan, and Dr. Vijay Kumar Foundation, 45 Bazaar Street, K. K. Nagar (West), Chennai 600078, India

Received February 4, 2004; Revised Manuscript Received March 3, 2004

ABSTRACT

Ten atom clusters of X = Si, Ge, Sn, and Pb are known to be magic, suggesting that addition of an atom to such clusters is generally unfavorable. However, here we report using an ab initio ultrasoft pseudopotential method that these clusters can be further stabilized by doping of a Ni or Pt atom, leading to some of the smallest metal encapsulated clusters of these elements. For Si and Ge, doping of Ni is optimal while for Sn and Pb, Pt is the best. Our results agree with the recent observations of strong abundances and magic nature of $X_{10}Co^-$ clusters of these elements. These findings could lead to the development of novel cluster-based nanomaterials for optoelectronic and other nanoscale applications.

Clusters of semiconducting materials are currently of great interest as these have an important role to play not only in the miniaturization of devices but also in the fundamental understanding of materials at the nanoscale. Clusters with novel properties such as enhanced stability by suitable doping, tunable gaps, and magnetic properties could lead to novel nanoscale optoelectronic as well as miniature spintronic and storage devices. The recent findings[1-6] of metal (M) encapsulated clusters of Si and Ge have generated much interest in this field and could lead to new possibilities of Si- and Ge-based nanomaterials. The M encapsulated clusters can be very symmetric with much higher band gaps that lie in the visible region in some cases.[7] These properties may extend their usage in photonics that could be combined with electronics to lead to new optoelectronic devices. It has been further shown that these clusters could be assembled to form nanotubes[8-10] of Si and Ge with novel magnetic properties such as high magnetic moments and piezomagnetic effect[11] at the nanoscale. Following these findings, there is a growing interest[12-15] in the field of M encapsulated clusters and their nanotubes[16] in order to explore their properties as well as new possibilities both theoretically and experimentally.

Recently, anion binary clusters of Co/Ge, Co/Sn, and Co/Pb have been produced[17] by laser ablation with high abundance of $X_{10}M^-$ clusters followed by a minimum for $X_{11}M^-$. There is an extraordinary peak in the mass distribution for $Ge_{10}Co^-$. The ground state of these clusters is predicted[18] to be a bicapped tetragonal antiprism. However, why these clusters exhibit magic behavior with such a large abundance is not understood. Here we explain the unusual stability of these charged clusters and explore several binary combinations to predict new magic clusters of Si, Ge, Sn, and Pb with 10 atoms doped with Ni, Pd, or Pt. These are the smallest caged clusters of these elements doped with a transition (T) M atom. Si and Ge clusters are important for semiconductor devices while Sn and Pb are useful for soldering. Doping of M atoms provides a nice way to manipulate their properties at the nanoscale.

In $Ge_{10}Co$ anions Co atom can be replaced by the next element, namely Ni to obtain neutral clusters. As the size of the M atom plays an important role[1-3] in the stability and structures of M encapsulated Si or Ge clusters, we explore the optimal combinations among the TM and group-14 elements in order to find the most stable clusters. Si_{10}, Ge_{10}, Sn_{10}, and Pb_{10} are known to be magic with high abundances[17,19] and have compact structures[20] unlike the relatively open bulk diamond structure of Si, Ge, and Sn. All these clusters also have large highest occupied–lowest unoccupied molecular orbital (HOMO–LUMO) gaps (Table 1) that decrease in going from Si to Pb. Therefore, it would appear difficult to transform such magic clusters into other magic clusters by doping of an atom, as by definition of magic clusters, addition of one more atom of the constituent is less favorable. However, it is possible that a different isomer of

* Corresponding author. Vijay Kumar, Institute for Materials Research, Tohoku University, Katahira 2-1-1, Aoba-ku, Sendai 980-8577 Japan. Phone: 81-22-215-2287. Fax: 81-22-215-2052. E-mail: kumar@imr.edu.
† Tohoku University.
‡ Dr. Vijay Kumar Foundation.

10.1021/nl0498076 CCC: $27.50
Published on Web 03/20/2004

Table 1. Binding Energies (BEs) and HOMO−LUMO Gaps of the Lowest Energy Isomers of X_{10} and M Doped Clusters

	BE (HOMO−LUMO gap) (eV)			
X	X_{10}	Ni	Pd	Pt
Si	3.85 (2.09)	3.95 (1.94)	3.81 (1.70)	3.94 (1.29)
Ge	3.35 (1.94)	3.55 (1.66)	3.34 (1.46)	3.52 (1.54)
Sn	2.91 (1.54)	3.15 (1.24)	3.06 (1.17)	3.24 (1.30)
Pb	2.69 (0.90)	2.92 (0.84)	2.86 (0.95)	3.04 (1.06)

the same cluster gets stabilized by doping. Recently, doping of Si, Ge, and Sn clusters with divalent M atoms was shown[21] to lead to such a behavior. In particular, Be doping enhances significantly the stability of the elemental magic clusters of these elements in a different structure and also changes some nonmagic clusters into magic ones. From the point of view of usage, Be is not favored because of its toxic nature. On the other hand, TM atoms are particularly important[7] for the stability of M encapsulated Si and Ge clusters. Therefore, the finding of large abundances of $X_{10}Co^-$ is significant. It is possible that the d level of the M atom is fully occupied and it behaves like the closed shell divalent M atoms. Therefore, the magic nature of the X_{10} cluster can be retained if the HOMO−LUMO gap remains significant.

$Ge_{10}Co^-$ has been shown[18] to have a large HOMO−LUMO gap, while we find that the neutral $Ge_{10}Co$ cluster has a significantly reduced gap of 0.23 eV only. For the stability of the neutral clusters it is important that these have large HOMO−LUMO gaps. The exceptional stability of $Ge_{10}Co^-$ and large HOMO−LUMO gap therefore arise due to the charged nature of these clusters. It is also noteworthy that cation $Ge_{10}Co$ does not show high abundance. For neutral clusters, we choose Ni as it has 10 valence electrons in $3d^94s^1$ configuration. In the doped cluster, it is possible that the 4s electron is transferred to the 3d level. If so, it is further important to find the optimal combination of TM atom in the same column and the group 14 elements.

The optimizations have been performed using an ab initio ultrasoft pseudopotential plane wave method[22] and the conjugate gradient technique with the generalized gradient approximation (GGA) for the exchange-correlation energy. The cutoff energy for the plane wave expansion is taken to be 17.76, 14.63, and 14.07 Ry for Ni, Pd, and Pt doped clusters, respectively. The Brillouin zone is represented by the Γ-point. The structures are considered to be converged when the force on each ion becomes 0.01 eV/Å or less. We consider a few initial structures such as the one with the M atom at the center of a tetracapped trigonal prism (TTP) (lowest energy structure[20] for X_{10}, X = Si, Ge, and Sn), a bicapped tetragonal antiprism (close to the lowest energy structure for Pb_{10}), a bicapped cube, a decahedron, a pentagonal antiprism, and outside doping of TTP to explore the lowest energy structures. In Table 1, we have given the binding energies (BEs) and HOMO−LUMO gaps of X_{10} and the M doped clusters in the lowest energy structures.

Figure 1 shows four typical structures that are among the lowest energy structures for these clusters. For $Si_{10}Ni$, the lowest energy structure is one with a capped pentagon on

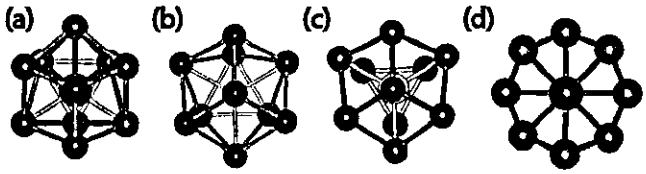

Figure 1. Representative lowest energy isomers of $X_{10}M$ clusters: (a) capped pentagon-rhombus structure (nearly 3-fold) as for $Si_{10}Ni$, (b) tetracapped trigonal prism as for $Pb_{10}Pt$, (c) a 3-fold symmetric structure as for $Si_{10}Pt$, and (d) bicapped square antiprism as for $Ge_{10}Ni$ and $Pb_{10}Pt$.

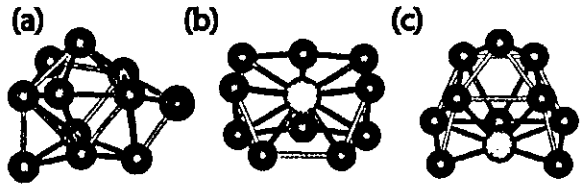

Figure 2. (a) Outside capping by the M atom as in $Si_{10}Pd$. Structures (b) and (c) show open structures for $Si_{10}Pt$ and $Ge_{10}Pt$, respectively.

one side of the Ni atom and a rhombus on the opposite side, as shown in Figure 1a. This is similar to the case of $Ge_{10}Co$ as well as to $Si_{10}Fe$ studied by Khanna et al.[13] However the HOMO−LUMO gap in $Si_{10}Ni$ is much larger with the value of 1.94 eV as compared to about 1 eV for $Si_{10}Fe$ showing that Ni doping is the most appropriate for the 10 atom Si magic clusters in agreement with the finding of large abundances of Co-doped anion clusters. This isomer is close to having 3-fold symmetry as it can be seen from the figure. An isomer with 3-fold symmetry is nearly degenerate and has the TTP structure with one triangular face opened up and Ni atom inside as shown in Figure 1b. The HOMO−LUMO gap is 1.98 eV. Since the GGA underestimates the gaps, the actual values are expected to be higher and to lie in the visible range. The magnetic moment of Ni atom gets completely quenched. An isomer with nearly 4-fold symmetry lies 0.77 eV higher in energy and acquires 2 μ_B magnetic moment in fully symmetric structure. The decahedral and pentagonal antiprism structures are found to have 2 μ_B magnetic moments in both the cases. Mpourmpakis et al.[13] also obtained a similar decahedral isomer for $Si_{10}Ni$. But it lies 0.67 eV higher in energy and has a small HOMO−LUMO gap of 0.33 eV. A decahedral structure was also obtained[13] for $Si_{10}Fe$. When a decahedral structure is optimized without spin-polarization, it transforms to a TTP structure with (surprisingly) slightly different bond lengths (Figure 1c) and it lies 0.27 eV higher in energy as compared to the lowest energy isomer. The HOMO−LUMO gap is also significantly different (1.49 eV). This structure has combined features of the pentagons and a capped hexagon as found in the fullerene-like and Frank−Kasper isomers[1] of the $Zr@Si_{16}$ cluster, respectively. A bicapped cube also changes to this isomer, whereas a bicapped square antiprism converts to the lower energy 3-fold structure (Figure 1b).

We also studied Ni outside Si_{10} on a triangular face of TTP. The converged structure (Figure 2a) lies 1.11 eV higher in energy. Therefore, Ni is favored inside the cage. The energy gain in doping Ni atom to Si_{10} is 5.13 eV, as

compared to the BE of 3.85 eV/atom for Si_{10}, and therefore the stability of Si_{10} cluster is enhanced by Ni doping (Table 1).

Doping of Pd in Si_{10} is favored outside (Figure 2a) with 1.70 eV HOMO−LUMO gap. A 3-fold structure (Figure 1c) lies 1.03 eV higher in energy with a 1.27 eV HOMO−LUMO gap. A decahedron with Pd inside opens up (Figure 2b). It lies 1.13 eV higher in energy with a HOMO−LUMO gap of 1.79 eV. It is to be noted that a similar structure for Ni lies 0.77 eV higher in energy than the lowest energy structure as the strain is reduced. A decahedron with 2 μ_B magnetic moment lies 1.5 eV higher in energy with a small HOMO−LUMO gap of 0.32 eV. Lu and Nagase[13] studied Os doping in Si_{10} and Ge_{10} and obtained open structures, showing that Os is not appropriate. The capped square antiprism structure converges to a slightly distorted (one square face becoming rectangular) decahedron. This structure lies 1.53 eV higher in energy with 1.34 eV HOMO−LUMO gap. The pentagon-rhombus isomer (Figure 1a) is almost degenerate with a 3-fold isomer (Figure 1b) and lies 1.71 eV higher in energy. These results show that Pd doping is unlikely inside Si_{10} as the gain in energy is only 2.48 eV. Outside doping may be possible with the energy gain of 3.49 eV.

The case of $Si_{10}Pt$ is, however, different. The lowest energy structure is a 3-fold isomer (Figure 1c). An isomer in which Pt opens the cage (Figure 2b) and is exposed for reactivity lies only 0.14 eV higher in energy. It also has a significant HOMO−LUMO gap of 1.32 eV. A capped square antiprism and a pentagonal antiprism also converge to this isomer. This isomer has rhombi in abundance. This tendency is also seen in another rather open structure (Figure 2c) which lies 0.41 eV higher in energy with 1.23 eV gap. A decahedron is stable with a magnetic moment of 2 μ_B and lies 0.57 eV higher in energy, similar to the case of Ni. The capped pentagon-rhombus structure lies 0.90 eV higher in energy with a significant gap of 1.67 eV and is very close to having 3-fold symmetry. Therefore, Pt doping is different from Ni and Pd. The gain in energy by Pt doping in the lowest energy structure is 4.83 eV and therefore, it also enhances the stability of Si_{10} but the HOMO−LUMO gap is significantly reduced to 1.29 eV as compared to 2.09 eV for Si_{10}.

As the atomic size of Ge is about 4% bigger than Si, the lowest energy structure of $Ge_{10}Ni$ is a capped square antiprism (Figure 1d), in contrast to the Si case for which it is unstable. The HOMO−LUMO gap is 1.66 eV, which is the highest among all the geometries studied for this cluster but smaller than the value for Ge_{10}. A bicapped cube also converges to this structure. A TTP structure (Figure 1b) is nearly degenerate and has a 1.67 eV HOMO−LUMO gap. The next lowest energy structure is decahedral and it lies 1.37 eV higher in energy with 2 μ_B magnetic moment. Ni atom is the optimal to stabilize this closed cage structure with very little elongation in Ge−Ge bond lengths as compared to the Ge_{10} cluster. The Ge−Ni bonds are shorter (2.44 Å) than the sum of the covalent radii of Ge and Ni. Therefore, it has significantly higher BE as compared to other isomers. The energy gain by Ni doping is 5.56 eV similar to silicon. However, the BE of Ge clusters is significantly lower as compared to Si clusters, and therefore the improvement in stabilization is more significant (Table 1), which makes it exceptional.

To optimize the HOMO−LUMO gap and the effect of the size of the dopant in the same group, we further studied $Ge_{10}Pd$ in different geometries. The lowest energy structure is similar to $Si_{10}Ni$ (Figure 1a) and the energy gain is 3.26 eV, which is more than the value for the Si cage as the strain in Ge is reduced. Therefore, going down from Si to Ge and Ni to Pd in the same column retains similar behavior, but the BE in the case of Pd decreases due to its closed shell atomic electronic structure. The TTP structure also converges to this isomer. Another isomer in which Pd is outside the Ge_{10} cluster (Figure 2a) is nearly degenerate while a distorted structure and the 3-fold symmetric structure (Figure 1c) lie 0.30 eV higher in energy. Therefore, Pd doping in Ge_{10} is not favorable as it is also the case for Si_{10}. Continuing further with $Ge_{10}Pt$, we find that the lowest energy structure is the same as for $Ge_{10}Pd$ (Figure 1a). However, the gain in energy of Ge_{10} due to doping is 5.26 eV. The hybridization of Pt orbitals with those of the Ge cage is better and it enhances the stability of Ge_{10}. The HOMO−LUMO gap in this case is 1.54 eV and similar to $Ge_{10}Ni$; this cluster should be strongly abundant. The Ge−Ge and Ge−Pt bond lengths increase by about 4% as compared to Ge_{10}. But the similar gain in energy as for Ni shows that the interaction of Pt with the cage is stronger. The 3-fold symmetric structure (Figure 1c) is nearly degenerate (0.08 eV higher) with 1.08 eV gap. The energy difference from the second lowest energy structure (Figure 1d) decreases to 0.39 eV while Pt outside Ge_{10} lies 0.54 eV higher in energy as compared to the lowest energy isomer. Therefore, Pt encapsulation also enhances the stability of Ge_{10} significantly.

Next we studied $Sn_{10}M$ (M = Ni, Pd, and Pt) clusters. Sn is significantly larger as compared to Si or Ge and has a tendency to be more metallic. Therefore, several of the structures (Figure 1a, b, and d) become nearly degenerate. The lowest energy structure for $Sn_{10}Ni$ is a bicapped square antiprism (Figure 1d) with a 1.23 eV HOMO−LUMO gap, which is slightly smaller as compared to the value for Sn_{10}. A 3-fold symmetric structure (Figure 1b) with slight distortion and the capped pentagonal-rhombus structure (Figure 1a) each lie only 0.06 eV higher in energy. Ni outside Sn_{10} lies 2.20 eV higher in energy. The same happens for Pd and Pt. Among these, the HOMO−LUMO gap is the largest (1.30 eV) for $Sn_{10}Pt$ in the lowest energy bicapped square antiprism structure. In this case also the Sn−Sn bond lengths are nearly the same as in Sn_{10} and so the strain due to doping is minimal. A similar trend is observed for Pb. The lowest energy structure for all M is a bicapped square antiprism (Figure 1e). In the case of Ni the HOMO−LUMO gap decreases to 0.84 as Ni is small and is not optimally bonded. But it increases to 0.99 eV for Pd and further to 1.06 eV for Pt. Therefore, we conclude that Pt is also the most optimally bonded in this case. The Pb−Pb bond lengths remain also nearly the same as in the lowest energy structure of Pb_{10}. This is also reflected from the energy gain which is 6.58

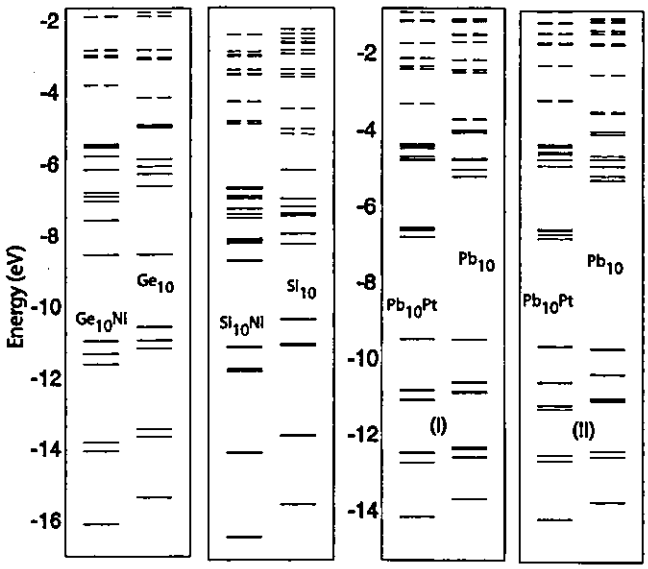

Figure 3. Kohn-Sham electronic states for different $X_{10}M$ and X_{10} (with the corresponding atomic positions) clusters. (I) and (II) are for the bicapped square antiprism and tetracapped trigonal prism isomers of $Pb_{10}Pt$, respectively.

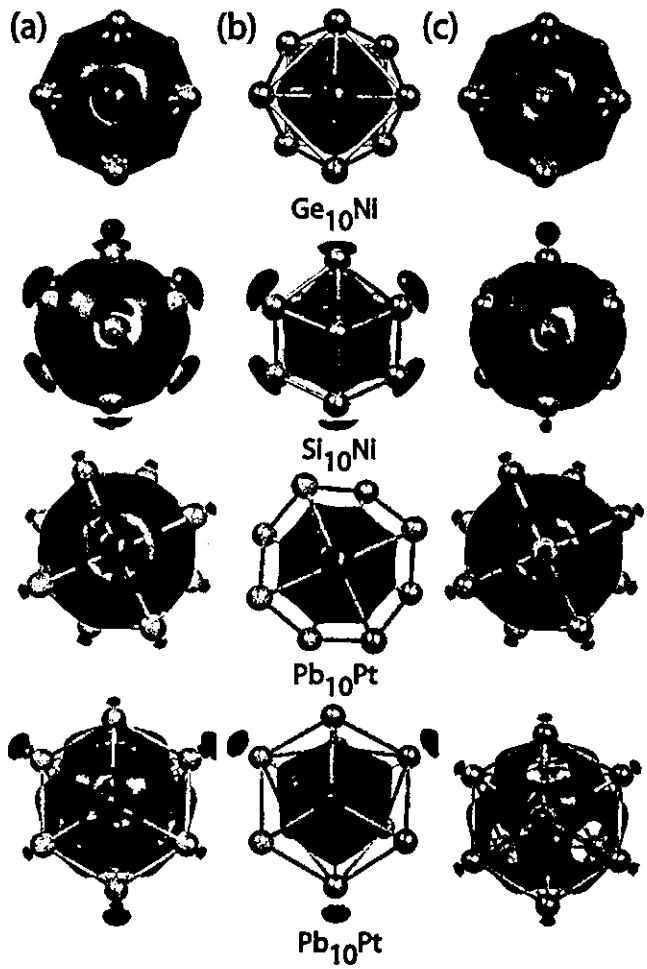

Figure 4. (a) Isosurface for the accumulation (red) and depletion (blue) of the electronic charge in $X_{10}M$ as compared to the isolated M and X_{10} with the same positions. Set (b) shows accumulation and (c) shows the depletion of charge separately.

and 6.52 eV for Sn and Pb, respectively. The gain in energy with Pd doping is 4.49 and 4.56 eV for Sn_{10} and Pb_{10}, respectively, while for Ni it is 5.54 and 5.21 eV, making Pt to be the best dopant for Sn_{10} and Pb_{10}.

These results show that Ni doped Si_{10} and Ge_{10}, and Pt doped Ge_{10}, Sn_{10}, and Pb_{10} clusters are optimal and are among the smallest TM atom encapsulated caged magic clusters of these tetravalent elements known so far. To understand the bonding nature we have shown in Figure 3 the Kohn–Sham energy states of the doped and undoped clusters keeping the same atomic configuration of the X atoms as in the doped cases. It is clear that most of the occupied states shift slightly to higher binding energies after doping, indicating that there could be small transfer of charge from the cage (Figure 4). The HOMO–LUMO gap for the distorted X_{10} cages reduces significantly as compared to the lowest energy structures. However, the states near the HOMO are significantly pushed down, whereas the LUMO of the X_{10} cage gets shifted upward, giving rise to a large gap as well as significant gain in energy leading to the stability of these clusters. Also comparing the states of X_{10} and $X_{10}M$ clusters, the covalently bonded d level of the TM atom forms the HOMO and is fully occupied. This supports our conjecture of the closed electronic d level in these magic clusters.

The electronic charge densities are shown in Figure 4 for the lowest energy structures of $Ge_{10}Ni$, $Si_{10}Ni$, and $Pb_{10}Pt$ clusters, which are among the best representative cases. The values of the isosurfaces have been kept to be the same in all cases for comparison. It is seen from the difference in the charge densities of the doped clusters and the overlapping densities of M and X_{10} with the corresponding positions as in $M@X_{10}$ that the charge is accumulated between the M atom and the X_{10} cage due to the covalent bonding. As we go down in the X column from Si to Pb, the charge accumulation decreases due to the more metallic character of bonding in these clusters. This is also reflected from the reduction in the depletion of charge from the X_{10} cage as well as smaller shift in the electronic states of $Pb_{10}M$ clusters (Figure 3).

In summary, we have systematically studied the $X_{10}M$ (X = Si, Ge, Sn, and Pb; M = Ni, Pd, and Pt) clusters and found some of the optimally M doped smallest magic clusters of the group 14 elements with 10 atoms. The stability of these clusters has been understood. We find that by suitably choosing X and M, the properties of these clusters can be tailored to optimize the stability as well as the HOMO–LUMO gap. $Si_{10}Ni$ shows the highest HOMO–LUMO gap of 1.96 eV, and this could be luminescent in the visible range. Sn and Pb clusters have the maximum stabilization energy. As we move down the group from Si to Pb, the enhancement in the stability of caged structures increases more by doping a bigger atom, such as Pt, because the strain due to the small size of the cage is reduced. Our results explain the stability and large abundances of $Ge_{10}Co^-$ clusters also while the best candidates for neutral clusters have been identified. These magic clusters with enhanced stabilities are likely to be produced in large quantities and can be used for making the assemblies of such clusters for nanoscale applications.

Acknowledgment. The authors thank the staff of the Center for Computational Material Science at the Institute for Materials Research for the use of Hitachi SR8000/64 supercomputing facilities. A.K.S. is grateful for the support of MEXT fellowship. V.K. acknowledges the hospitality at the Laboratory for Advanced Materials of the Institute for Materials Research.

References

(1) Kumar, V.; Kawazoe, Y. *Phys. Rev. Lett.* **2001**, *87*, 045503. Kumar, V.; Kawazoe, Y. *Phys. Rev. Lett.* **2003**, *91*, 199901 (E). Kumar, V. *Eur. Phys. J. D* **2003**, *24*, 227.
(2) Kumar, V.; Kawazoe, Y. *Phys. Rev. Lett.* **2002**, *88*, 235504.
(3) Kumar, V.; Kawazoe, Y. *Phys. Rev. B* **2002**, *65*, 073404.
(4) Kumar, V.; Kawazoe, Y. *Phys. Rev. Lett.* **2003**, *90*, 055502.
(5) Kumar, V.; Kawazoe, Y. *Appl. Phys. Lett.* **2002**, *80*, 859.
(6) Hiura, H.; Miyazaki, T.; Kanayama, T. *Phys. Rev. Lett.* **2001**, *86*, 1733.
(7) Kumar, V.; Briere, T. M.; Kawazoe, Y. *Phys. Rev. B* **2003**, *68*, 155412.
(8) Singh, A. K.; Kumar, V.; Briere, T. M.; Kawazoe, Y. *Nano Lett.* **2002**, *2*, 1243.
(9) Singh, A. K.; Briere, T. M.; Kumar, V.; Kawazoe, Y. *Phys. Rev. Lett.* **2003**, *91*, 146802.
(10) Singh, A. K.; Kumar, V.; Kawazoe, Y. *J. Mater. Chem.* **2004**, *14*, 555.
(11) Singh, A. K.; Kumar, V.; Kawazoe, Y., submitted for publication.
(12) Ohara, M.; Koyasu, K.; Nakajima, A.; Kaya, K. *Chem. Phys. Lett.* **2003**, *371*, 490.
(13) Lu, J.; Nagase, S. *Phys. Rev. Lett.* **2003**, *90*, 115506. Khanna, S. N.; Rao, B. K.; Jena, P.; Nayak, S. K. *Chem. Phys. Lett.* **2003**, *373*, 433. Lu, J.; Nagase, S. *Chem. Phys. Lett.* **2003**, *372*, 394. Mpourmpakis, G.; Froudakis, G. E.; Andriotis, A. N.; Menon, M. *J. Chem. Phys.* **2003**, *119*, 7498. Mpourmpakis, G.; Froudakis, G. E.; Andriotis, A. N.; Menon, *Phys. Rev. B* **2003**, *68*, 125407.
(14) Chen, Z.; Hirsch, A.; Nagase, S.; Thiel, W.; Schleyer, P. v R. *J. Am. Chem. Soc.* **2003**, *125*, 15507.
(15) Sen, P.; Mitas, L. *Phys. Rev. B* **2003**, *68*, 155404.
(16) Menon, M.; Andriotis, A. N.; Froudakis, G. E. *Nano Lett.* **2002**, *2*, 301.
(17) Zhang, X.; Li, G.; Gao, Z. *Rapid Commun. Mass Spectrom.* **2001**, *15*, 1573. Zhang, X.; Li, G.; Xing, X.; Zhao, X.; Tang, Z.; Gao, Z. *Rapid Commun. Mass Spectrom.* **2001**, *15*, 2399.
(18) Li, G.; Zhang, X.; Tang, Z.; Gao, Z. *Chem. Phys. Lett.* **2002**, *359*, 203.
(19) Kumar, V.; Esfarjani, K.; Kawazoe, Y. In *Clusters and Nanomaterials*; Kawazoe, Y., Kondow, T., Ohno, K., Eds.; Springer Series in Cluster Physics; Springer-Verlag: Heidelberg, 2002; p 9.
(20) Müller, J.; Liu, B.; Shvartsburg, A. A.; Ogüt, S.; Chelikowsky, J. R.; Siu, K. W. M.; Ho, K.-M.; Gantefor, G. *Phys. Rev. Lett.* **2000**, *85*, 1666. Ballone, P.; Andreoni, W.; Car, R.; Parrinello, M. *Phys. Rev. Lett.* **1988**, *60*, 271. Majumder, C.; Kumar, V.; Mizuseki, H.; Kawazoe, Y. *Phys. Rev. B* **2001**, *64*, 233405. Shvartsburg, A. A.; Liu, B.; Lu, Z.-Y.; Wang, C.-Z.; Jarrold, M. F.; Ho, K.-M. *Phys. Rev. Lett.* **1999**, *83*, 2167.
(21) Kumar, V.; Kawazoe, Y. *Appl. Phys. Lett.* **2003**, *83*, 2677.
(22) Kresse, G.; Furthmüller, J. *Phys. Rev. B* **1996**, *55*, 111 69.

NL0498076

journal

J. Am. Ceram. Soc., 87 [1] 166–69 (2004)

Oxygen-Deficient Anatase Precipitated from High-Temperature Plasma

Yoshikiyo Kato

Department of Material and Biological Chemistry, Yamagata University, Yamagata 990-8560, Japan

Hiroko Yokobayashi

Research Center for Higher Education, Tohoku University, Sendai 980-8576, Japan

Atsuo Kasuya

Center for Interdisciplinary Research, Tohoku University, Sendai 980-8578, Japan

Masahiro Kagawa* and Masashi Kawasaki

Institute for Materials Research, Tohoku University, Sendai 980-8577, Japan

Feeding atomized aqueous solutions containing $TiCl_4$ into an argon high-temperature inductively coupled plasma (ICP) resulted in the formation of mixtures of white and blue particles. The mixtures consisted of anatase and an extra phase of rutile. Adding oxygen to the ICP led to the production of a single phase of white anatase. The blue particles could be characterized as oxygen-deficient anatase. Electrophoretic mobility measurements indicated that Na^+ participated in determining the surface potential of the mixtures. The oxygen defects may provide the adsorption sites to Na^+.

I. Introduction

The high photocatalytic performance of titanium oxide under visible light has recently been achieved by doping nitrogen, carbon, and metal ions.[1–3] These dopings were performed by sputtering, combustion, and ionized cluster beam methods, respectively. Thus, various material processing techniques have contributed to the preparation of new materials.

A modification of spray pyrolysis with a high-temperature inductively coupled plasma (ICP) can be applied to the preparation of ultrafine oxide particles (the spray-ICP technique). In this method the liquid droplets completely decompose in the ICP to form a gas phase from which the oxide particles precipitate in a short time.

The properties of powders depend on particle shape, sizes and size distributions, additives, and defects, etc. With anatase, a particle size of 25–40 nm is optimum for high photocatalytic activities.[4] Metal ion doping affects the incident proton conversion efficiency of nanocrystalline electrodes.[5] Phosphates inhibit anatase from transforming to rutile by hindering the mobility of surface ions.[6]

In the present study, ultrafine particles of anatase have been prepared by the spray-ICP technique. Since liquid or suspension precursors were used, the anatase would occlude water. Phosphates, when co-precipitated, possibly affect the transformation to rutile. The anatase was obtained as mixtures of white and blue particles; the latter particles could be deficient in oxygen. Probably the oxygen defects determine the surface potential. These subjects will be clarified by X-ray diffraction, electron microscope observation, thermal analysis, diffuse reflectance spectroscopy, and electrophoretic mobility measurements.

II. Experimental Procedure

The solution and suspension precursors were prepared from $TiCl_4$ and H_3PO_4 (Wako Pure Chemicals) and distilled water. The solutions containing $TiCl_4$ (0.3 mol/L) were used to precipitate pure TiO_2. The suspensions as-prepared by mixing $TiCl_4$ and H_3PO_4 (0.1 mol/L nominal Ti concentration, 5 wt% H_3PO_4) were used to co-precipitate the phosphate. Figure 1 shows the experimental setup. The atomized precursor was introduced into an Ar-ICP (feed rate, 10–20 cm^3/h) through a narrow-tipped quartz nozzle (1.5–1.7-mm diameter) with an Ar carrier gas of 1.4 L/min. The ICP (40-mm diameter, 160-mm length) was generated at a frequency of 6 MHz and a running power of 5–6 kW and was stabilized with an Ar cooling gas of 30 L/min. The precipitation conditions were made oxidative by adding 6–8 mol% O_2 into the cooling gas. This required a running power of 7–8 kW. Introduction of the precursor generated a tail flame of 600 mm long. The particles were precipitated on the wall of a Pyrex glass tube (110-mm diameter and 600-mm length) placed under the ICP and also using an electrostatic precipitator connected to the glass tube. The particles were characterized by X-ray diffraction (XRD; Rigaku, Cu$K\alpha$ radiation with Ni filter and single graphite monochromator), transmission electron microscope observation (TEM; JEOL, JM3010), thermogravimetric and differential thermal analysis (TGA and DTA; Ulvac-Shinkuriko, MTS-9000, heating rate of 10°C/min, in air), diffuse reflectance spectroscopy (DRS: Hitachi, UV-spectrometer 330, integration sphere 210-2101, $BaSO_4$ sample holder of 3-mm diameter), and microscope electrophoresis (magnification, 150; dark field illumination; in 1×10^{-3} mol/L $NaClO_4$ or tetra-*n*-butylammonium perchlorate ($(n\text{-}Bu)_4NClO_4$) electrolytes; pH adjustment with $HClO_4$, NaOH, and/or $(n\text{-}Bu)_4NOH$ (Nacalai); particles were suspended around neutral pH).

III. Results and Discussion

Table I summarizes the colors and phases of the powders precipitated on the glass-tube wall and in the electrostatic precipitator.

R. H. French—contributing editor

Manuscript No. 10361. Received July 5, 2003; approved August 18, 2003.
*Member, American Ceramic Society.

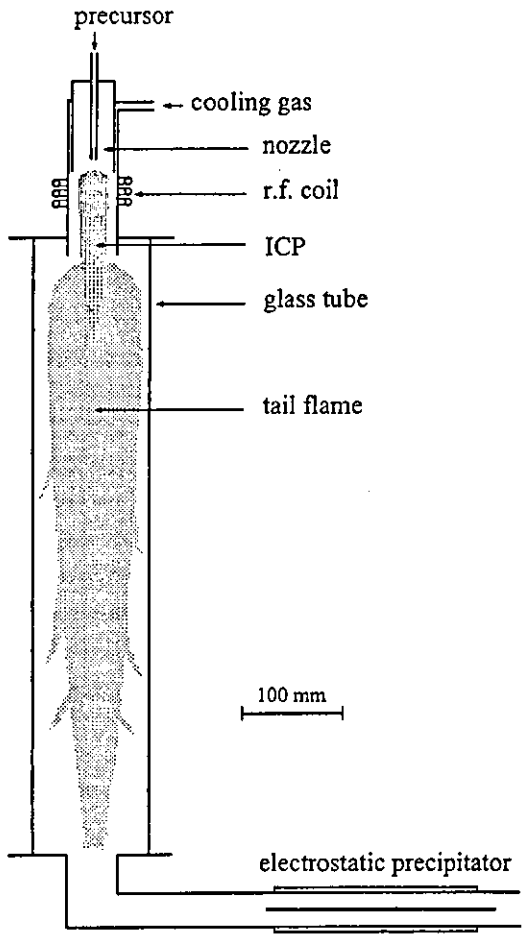

Fig. 1. Experimental setup.

The powder precipitated on the glass-tube wall from the Ar-ICP (experiment 1, Ar-g) contained white and blue particles (about 1:1 in volume ratio), whereas that precipitated in the electrostatic precipitator (Ar-e) held only white particles. XRD indicated that Ar-g and Ar-e both consisted of anatase and an extra phase of rutile (ratio in highest XRD peak; 101-anatase:110-rutile ≅ 6:1 for Ar-g and 14:1 for Ar-e). TEM revealed that Ar-g and Ar-e were composed of spherical particles. With the particle size, however, Ar-g had a wider particle size distribution (10–50 nm) than Ar-e (10–30 nm).

The precipitation from the oxidative conditions (experiment 2) resulted in the formation of white particles that were characterized as a single phase of anatase (O_2-g and O_2-e). Hence, the blue particles contained in Ar-g can be identified as oxygen-deficient anatase.

In the co-precipitation of the phosphate (experiment 3), P-g was obtained as a mixture of white and blue particles. Its phase was, however, only anatase. This differs from Ar-g. After all, the co-precipitation of the phosphate did not affect the oxygen deficiency but promoted the formation of anatase.

The particle size and phase of the powders depended on the precipitator. The particles may be roughly divided into two groups based on where and how they condense from the ICP. The first group is the particles condensed from the surface of the tail flame in the direction perpendicular to the flame axis, and the second group is those condensed at the flame tip. The glass-tube wall precipitates most of the particles of the first group, whereas the electrostatic precipitator traps those of the second group. The glass tube encloses the tail flame so close that part of the tail flame is rapidly cooled, resulting in the formation of small particles. In the tail flame, turbulence flows are inclined to occur. These flows are maintained at high temperatures for a long time. The particles involved in these flows grow large because the chance of coalescence is high. Additionally, the succeeding crystal growth is often promoted, accompanying the formation of a high-temperature form of isomorphs, i.e., rutile. After all, with the powders precipitated on the glass-tube wall, the particle size distributes in a wide range and the content of rutile becomes high. At the tail flame tip, the particles condense under relatively homogeneous precipitation conditions, and they are carried away to the electrostatic precipitator immediately after the condensation. This leads to the formation of particles with a narrow particle size distribution.

The blue particles were contained only in the powders precipitated on the glass-tube wall (Ar-g and P-g), implying that they were formed by rapid quenching of the tail flame. Probably their crystal growth ceased before the stoichiometric composition of anatase was formed. Under the oxidative precipitation conditions, the stoichiometric composition could be achieved because of the high concentration of oxygen (O_2-e and O_2-g).

Figure 2 shows TGA and DTA of Ar-g before (a) and after (b) being dried at room temperature. Before being dried, Ar-g exhibited two large weight loss steps in the temperature range up to about 500°C. Since the aqueous precursors were used, Ar-g occludes water. The first step is assigned to the release of the water adsorbed on the particle surface, and the second one is to that of the water staying in the lattice. Above 600°C a small amount of weight gain occurred. When Ar-g was quenched at 450°C, its color was found to have already changed from blue to yellow. Clearly the oxygen defects were partly filled. Consequently, the weight gain above 600°C is due to the uptake of oxygen. Reasonably, the dried Ar-g revealed a smaller weight loss below 500°C, so a larger amount of weight gain above 530°C resulted. The main DTA profile corresponded to the endothermic and exothermic reactions of the water releases and oxygen uptake. The noiselike profile suggests that the particles are so small that they move in the DTA cell.

TGA revealed a plateau in the temperature range of 430°–530°C (Fig. 2(a)). Apparently Ar-g contains 4.1% (=2.0 + 2.1) water and 0.7% oxygen deficiency. The previously dried Ar-g is expected to exhibit 0.72% (=0.7 × 100/95.9) oxygen uptake. However, the apparent uptake was 2.5% (Fig. 2(b)), which is much larger than the expected weight increase. This discrepancy can be explained in terms of duplication of weight loss and gain. That is, the releases of water and the oxygen uptake occur simultaneously in the plateau temperature range. As cited above, the color change of Ar-g quenched at 450°C supports the occurrence of the oxygen uptake.

The transformation of anatase to rutile increased with increasing temperature. At 450°C the rutile content against anatase in the XRD peak intensity was found to have already increased, and at 1050°C the complete conversion to rutile was ascertained. The co-precipitation of the phosphate hindered this transformation. The anatase of P-g was retained up to nearly 1000°C. Mechanically mixed phosphates cannot retain anatase at such high temperatures, and only the phosphate chemisorbed on TiO_2 as a bidentate ligand can block the transformation by inhibiting the surface ion mobility.[6] The phosphate in the present study is likely to stabilize the anatase through the same mechanism. In other words, the phosphate settles on the particle surface in the precipitation process. On the oxygen uptake, however, the phosphate had no effect. P-g changed to white when heated for 15 min at 400°C.

Figure 3 shows the DRS of Ar-g (a), Ar-g quenched at 450° (b) and at 1050°C (c), and commercial anatase quenched at 1050°C (d). Ar-g had two absorption bands, one at 450–500 nm and the other above 500 nm. The absorption edge was around 390 nm, which is almost equal to that of ordinary anatase. At 450°C, the bands weakened and the absorption edge red-shifted. At 1050°C, the absorption edge red-shifted further to 415 nm and the two bands almost disappeared. The absorption edge was almost the same as that of the commercial anatase quenched at 1050°C. However, the former was light yellow, whereas the latter was white. The oxygen uptake of Ar-g was not completed even at 1050°C. This is reflected in their DRS spectra. Ar-g quenched at 1050°C had a continuous weak absorption band above 400 nm,

Table I. Colors and Phases of Powders Precipitated on the Glass Tube Wall (Glass) and in Electrostatic Precipitator (Electrostatic)

Experiment	Precursor	Cooling gas	Colors and phases†	
			Glass	Electrostatic
1	$TiCl_4$	Ar	Blue + white (Ar-g), anatase + rutile	White (Ar-e), anatase + rutile
2	$TiCl_4$	Ar + O_2	White (O_2-g), anatase	White (O_2-e), anatase
3	$TiCl_4$ + H_3PO_4	Ar	Blue + white (P-g), anatase	White (P-e), anatase

†Parentheses indicate names of powders used in text.

whereas the commercial anatase quenched at the same temperature revealed no absorption band there.

Figure 4 shows the mobility (U; $(\mu m \cdot s^{-1})/(V \cdot cm^{-1})$) vs pH of O_2-e (a) and Ar-g (b) measured in the $NaClO_4$ electrolyte, and Ar-g measured in the $(n\text{-}Bu)_4NOH$ electrolyte (c). In the $NaClO_4$ electrolyte, as pH increased, the mobility of O_2-e shifted gradually in the negative direction, having an isoelectric point (iep) at pH 6. This iep was almost equal to reported values,[7,8] implying that O_2-e is an ordinary defect-free anatase. The mobility of Ar-g exhibited a yoyo-ing pH dependence with a positive shift between pH 6 and 10. This shift did not appear in the $(n\text{-}Bu)_4NClO_4$ electrolyte. Reasonably Na^+ causes the positive shift. Since Ar-g contains the blue particles that have oxygen defects, Na^+ is likely to interact with the defects and determine the particle surface.

We will describe the mobility vs pH of Ar-g measured in the $NaClO_4$ electrolyte in terms of the surface charge density based on a simplified model of Ref. 9. At the solid liquid interface, protons are bound to negatively charged metal oxide ions (A^-) to provide positive sites (AH_2^+) in the high-pH region. With increasing pH, AH_2^+ dissociates stepwise to give neutral (AH) and negative sites, A^-. There must be the following equilibrium relations among these sites:

$$AH_2^+ \overset{K_+}{\rightleftharpoons} AH + H^+ \tag{1}$$

$$AH \overset{K_-}{\rightleftharpoons} A^- + H^+ \tag{2}$$

The respective dissociation constants for Eqs. (1) and (2), K_+ and K_-, are given by Eqs. (3) and (4):

$$K_+ = \frac{[AH]_{sf}[H^+]}{[AH_2^+]_{sf}} \tag{3}$$

$$K_- = \frac{[A^-]_{sf}[H^+]}{[AH]_{sf}} \tag{4}$$

where the square brackets with a suffix of "sf" represent the surface concentrations of the species involved per unit area at the interface. $[H^+]$ is the concentration of the proton in the solution.

Further, Ar-g has the oxygen defects that are equilibrated with Na^+:

$$A^* + Na^+ \overset{K'}{\rightleftharpoons} A^*{\cdot}Na^+ \tag{5}$$

where A^* represents the oxygen defect sites in equilibrium with Na^+. K' is an association constant given by

$$K' = \frac{[A^*{\cdot}Na^+]_{sf}}{[A^*]_{sf}[Na^+]} \tag{6}$$

where $[Na^+]$ is the concentration of Na^+ in the solution.

The total site arising from Eqs. (1) and (2) is c_1, and that from Eq. (5) is c_2,

$$c_1 = [AH_2^+]_{sf} + [AH]_{sf} + [A^-]_{sf} \tag{7}$$

$$c_2 = [A^*]_{sf} + [A^*{\cdot}Na^+]_{sf} \tag{8}$$

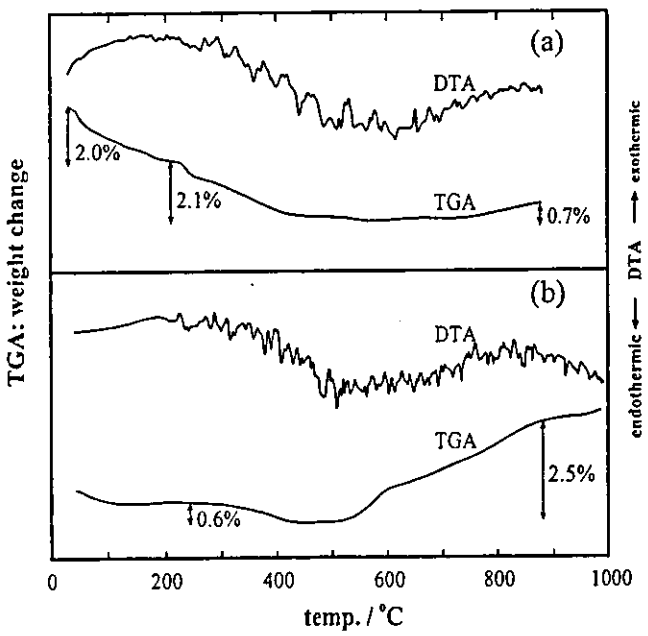

Fig. 2. TGA and DTA of Ar-g before (a) and after (b) being dried.

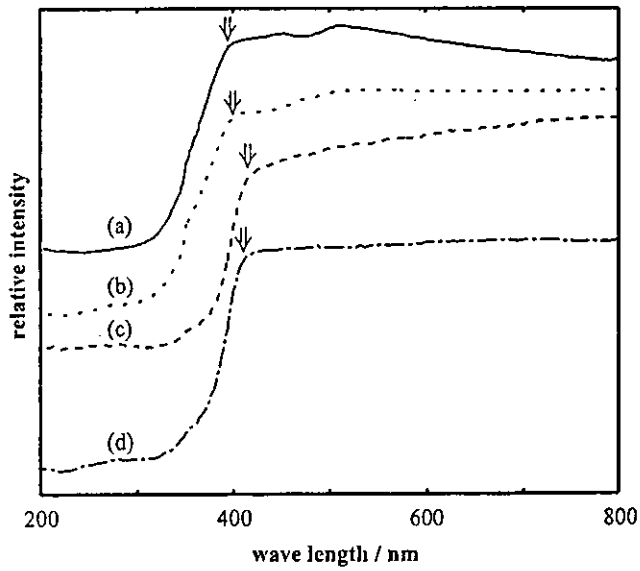

Fig. 3. DRS of Ar-g (a), Ar-g quenched at 450° (b) and at 1050°C (c), and commercial anatase quenched at 1050°C (d). ⇓ indicates the absorption edge.

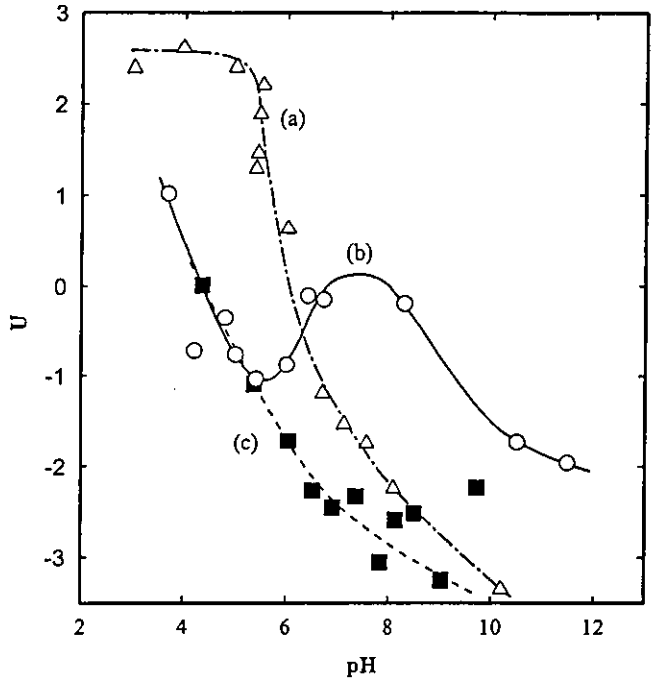

Fig. 4. *U* vs pH of O_2-e measured in $NaClO_4$ (a), of Ar-g in $NaClO_4$ (b), and of Ar-g in $(n\text{-Bu})_4NOH$ electrolyte (c).

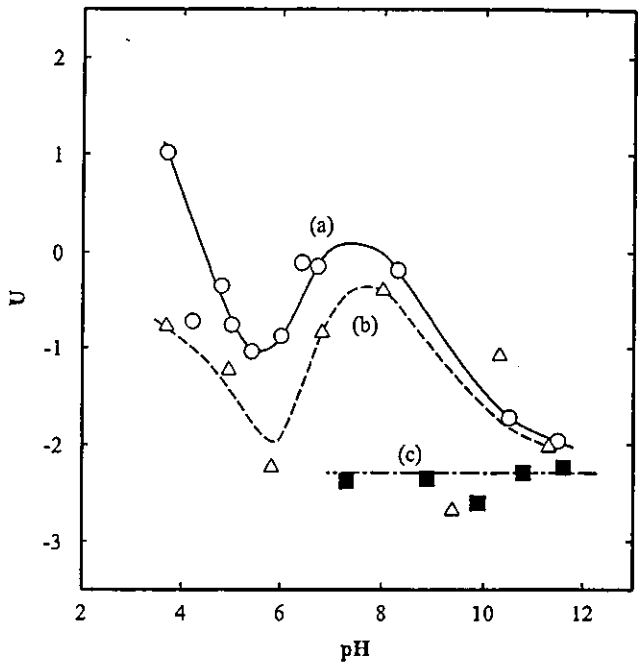

Fig. 5. *U* vs pH measured in $NaClO_4$: Ar-g (a), Ar-g after being water-washed (b), and Ar-g after being dispersed into NaOH (c).

in all, the surface charge density, σ, can be represented by

$$\sigma = [AH_2^+]_{sf} + [A^*{\cdot}Na^+]_{sf} - [A^-]_{sf}$$

$$= \frac{c_1}{1 + \dfrac{K_+}{[H^+]} + \dfrac{K_+K_-}{[H^+]^2}} + \frac{c_2}{\dfrac{[H^+]}{K'K_W} + 1} - \frac{c_1}{\dfrac{[H^+]^2}{K_+K_-} + \dfrac{[H^+]}{K_-} + 1} \tag{9}$$

where K_W is the ion product for water ($[H^+][OH^-] = 10^{-14}$).

Since the mobility is a function of the surface charge density, the mobility vs pH can be explained in terms of the dependence of σ on $[H^+]$ in Eq. (9). The mobility took a positive value at pH 4. As pH increased, the mobility decreased and shifted in the positive direction between pH 6 and 10. This finding indicates that there must be the following relation among the equilibrium constants.

$$K_+ > \frac{1}{K'K_W} > K_- \tag{10}$$

The values roughly estimated from curve fitting were as follows: K_+, in the order of 10^{-4}; K', 10^8; and K_-, 10^{-10}; $c_1{:}c_2 \cong 2{:}1$. The high K' value indicates that the oxygen defects have a strong affinity to Na^+.

Figure 5 shows the effect of some treatments for Ar-g on the mobility vs pH measured in the $NaCl_4$ electrolyte: Ar-g (a), Ar-g after being water-washed (b), and Ar-g after being dispersed in a NaOH solution of pH = 12 (c). The positive mobility shift observed between pH 6 and 10 could still be seen even after the specimen was water-washed. However, the shift did not appear on dispersion into the NaOH solution, indicating that the reverse reaction in Eq. (5) becomes slow. Thus, the oxygen defects interact with Na^+, and under certain conditions the Na^+ can firmly be held in the anatase.

IV. Summary

The titanium oxide powders prepared by the spray-ICP technique were composed of white and blue particles; the latter particles were characterized as oxygen-deficient anatase. On heating, the powders absorbed oxygen with the red-shift of the absorption edge and also with the transformation to rutile. In solutions containing Na^+, the oxygen defects provide adsorption sites to Na^+, participating in determining the surface potential.

Acknowledgments

The authors wish to thank Emeritus Professor of Tohoku University, Dr. S. Usui, for many helpful discussions.

References

[1]R. Asahi, T. Morikawa, T. Ohwaki, K. Aoki, and Y. Taga, "Visible Light Photocatalysis in Nitrogen-Doped Titanium Oxides," *Science (Washington, D.C.)*, 293, 269–71 (2001).

[2]S. U. M. Khan, M. Al-Shahry, and W. B. Inger Jr., "Efficient Photochemical Water Splitting by a Chemically Modified n-TiO_2," *Science (Washington, D.C.)*, **297**, 2243–45 (2002).

[3]H. Yamashita, M. Harada, J. Misaka, M. Takeuchi, Y. Ichihashi, F. Goto, M. Ishida, T. Sasaki, and M. Anpo, "Application of Ion Beam Techniques for Preparation of Metal Ion-Implanted TiO_2 Thin Film Photocatalyst Available under Visible Light Irradiation: Metal Ion-Implantation and Ionized Cluster Beam Method," *J. Synchrotron Radiat.*, **8**, 569–71 (2001).

[4]C. B. Almquist and P. Biswas, "Role of Synthesis Method and Particle Size of Nanostructured TiO_2 on Its Photoactivity," *J. Catal.*, **212** [2] 145–56 (2002).

[5]Y. Wang, H. Cheng, Y. Hao, J. Ma, W. Li, and S. Cai, "Photoelectrochemical Properties of Metal-Ion-Doped TiO_2 Nanocrystalline Electrodes," *Thin Solid Films*, 349, 120–25 (1999).

[6]J. Criado and C. Real, "Mechanism of the Inhibiting Effect of Phosphate on the Anatase → Rutile Transformation Induced by Thermal and Mechanical Treatment of TiO_2," *J. Chem. Soc., Faraday Trans. 1*, 79, 2765–71 (1983).

[7]M. M. Soltys, Z. M. Yaremko, N. H. Tkachenko, and V. D. Havryliv, "Poly(methacrylic acid) Adsorption and Electrical Surface Properties of Titanium Dioxide Suspensions," *Adsorpt. Sci. Technol.*, **20** [7] 633–45 (2002).

[8]G. R. Wiese and T. W. Healy, "Adsorption of Al(III) at the TiO_2–H_2O Interface," *J. Colloid Interface Sci.*, **51** [3] 434–42 (1975).

[9]D. E. Yates, S. Levine, and T. W. Healy, "Site-Binding Model of the Electrical Double Layer at the Oxide/Water Interface," *J. Chem. Soc., Faraday Trans. 1*, **70**, 1807–18 (1977). □

Ultra-stable nanoparticles of CdSe revealed from mass spectrometry

ATSUO KASUYA*[1], RAJARATNAM SIVAMOHAN[1], YURII A. BARNAKOV[1], IGOR M. DMITRUK[1], TAKASHI NIRASAWA[2,3], VOLODYMYR R. ROMANYUK[1], VIJAY KUMAR[1,4,5], SERGIY V. MAMYKIN[1], KAZUYUKI TOHJI[2], BALACHANDRAN JEYADEVAN[2], KOZO SHINODA[2], TOSHIJI KUDO[3], OSAMU TERASAKI[6], ZHENG LIU[6], RODION V. BELOSLUDOV[4], VIJAYARAGHAVAN SUNDARARAJAN[1,7] AND YOSHIYUKI KAWAZOE[4]

[1]Center for Interdisciplinary Research, Tohoku University, Sendai, 980-8578, Japan
[2]Graduate School of Environmental Studies, Tohoku University, Sendai, 980-8579, Japan
[3]Bruker Daltonics K.K., Kanagawa-ku, Yokohama, 221-0022, Japan
[4]Institute for Materials Research, Tohoku University, Sendai, 980-8577, Japan
[5]Dr Vijay Kumar Foundation, Chennai, 600 078, India
[6]Department of Physics, Tohoku University, Sendai, 980-8578, Japan
[7]Centre for Development of Advanced Computing, Pune, 411 007, India
*e-mail: kasuya@cir.tohoku.ac.jp

Published online: 25 January 2004; doi:10.1038/nmat1056

Nanoparticles under a few nanometres in size have structures and material functions that differ from the bulk because of their distinct geometrical shapes and strong quantum confinement. These qualities could lead to unique device applications. Our mass spectral analysis of CdSe nanoparticles reveals that $(CdSe)_{33}$ and $(CdSe)_{34}$ are extremely stable: with a simple solution method, they grow in preference to any other chemical compositions to produce macroscopic quantities. First-principles calculations predict that these are puckered $(CdSe)_{28}$-cages, with four- and six-membered rings based on the highly symmetric octahedral analogues of fullerenes, accommodating either $(CdSe)_5$ or $(CdSe)_6$ inside to form a three-dimensional network with essentially heteropolar sp^3-bonding. This is in accordance with our X-ray and optical analyses. We have found similar mass spectra and atomic structures in CdS, CdTe, ZnS and ZnSe, demonstrating that mass-specified and macroscopically produced nanoparticles, which have been practically limited so far to elemental carbon[1], can now be extended to a vast variety of compound systems.

Single-sized, stable nanoparticles are highly valuable because they have well-defined structures that can be identified with atomic precision. Their specific physical and chemical properties can be analysed, or realised, on the basis of their particular atomic arrangements. Such assemblies of atoms may serve as versatile building blocks for functional materials in nanometre science and technology. Recent extensive studies show that they could be produced not just in carbon but in other elements and compounds that may have electronic, optical and medical applications: examples are metal-encapsulated Si clusters[2], polyhedral-shell-like BN[3,4], and size- or shape-controlled II–VI compounds[5–7]. Here we report the synthesis and identification of mass-selected $(CdSe)_{33}$ and $(CdSe)_{34}$ nanoparticles in solution. These constitute the first compound nanoparticles that are stable and macroscopically produced at precisely specified numbers of constituent atoms with their stoichiometric composition identical to the bulk solids.

$(CdSe)_n$ nanoparticles were prepared in reverse micelles (see Methods). The sample in toluene was dried on the target plate of a time-of-flight mass spectrometer equipped with a nitrogen laser. Curve 1 in Fig. 1 shows the mass spectrum of positive ions from this sample produced by laser vaporization without cooling by carrier gas injection in the vacuum chamber. It shows three dominant peaks at $n = 13, 33$ and 34 with 1:1 stoichiometry of Cd/Se as in the bulk, together with much weaker peaks for off-stoichiometric particles. The peak width represents binomial isotope distributions of naturally abundant Cd and Se atoms. The intensities of the peaks at 33 and below tend to increase relative to 34 as the laser power increases, indicating that particles of $n < 33$ may also be produced by fragmentation of 33 and 34. The characteristic feature of curve 1 is that only the two peaks at $n = 33$ and 34 appear prominently in a region of the plot that covers a very wide range of mass (more than 19 CdSe units), indicating that only $(CdSe)_{33}$ and $(CdSe)_{34}$ are grown in the solution because of their extremely selective stabilities. From atomic force microscopy (AFM) measurement of the step height on a few-monolayer film deposited on graphite, we determined the diameter of these nanoparticles to be 1.5 nm.

To see the stability of these nanoparticles further, we measured mass spectra from laser ablation of bulk crystalline samples of CdSe, CdS, ZnS and ZnSe. They all show appreciable peaks at $n = 13, 33$ and 34, which are produced even in the violent ablation process, which would be expected to fragment the clusters into lower-mass particles. This indicates the extreme stability of particles at $n = 33$ and 34 without ligands as noted in

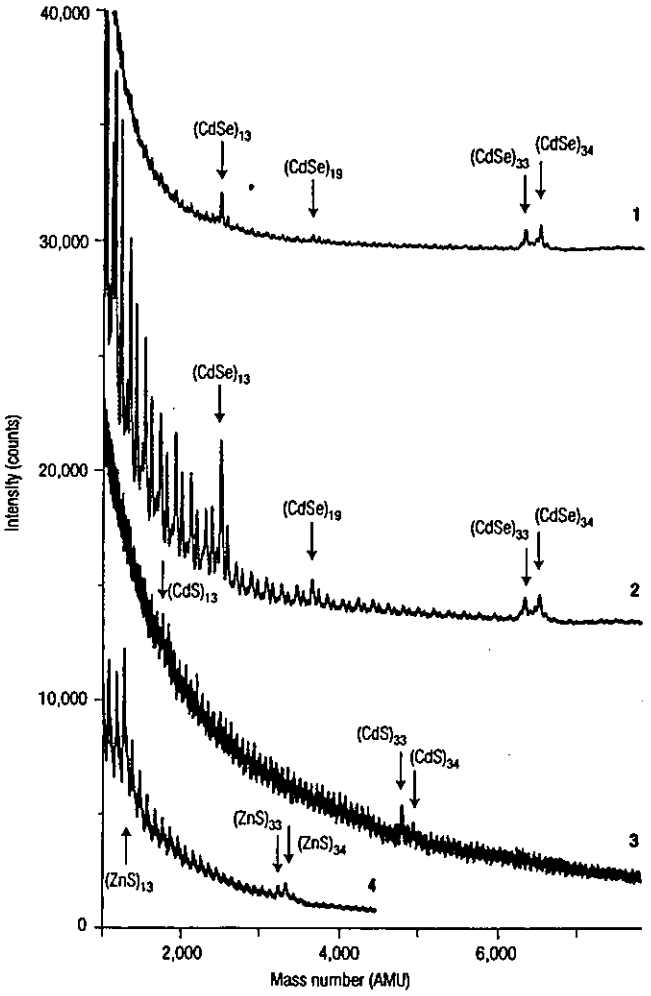

Figure 1 Time-of-flight mass spectra of positive ions. Curve 1 is for nanoparticles of CdSe prepared in toluene. Other mass spectra are produced by laser ablation of bulk powders of CdSe (curve 2), CdS (curve 3) and ZnS (curve 4).

curves 2, 3 and 4 of Fig. 1, which show CdSe, CdS and ZnS, respectively. Martin[8] finds a similar tendency for ZnS with helium gas cooling during ablation.

Measurements of optical absorption in solution give additional evidence that our sample contains stable mass-selected nanoparticles. Curve 1 of Fig. 2 has a sharp excitonic peak at 415 nm together with smaller peaks at 382 nm and 352 nm, blueshifted considerably from the bulk value of 680 nm. This indicates that the solution contains only specific sizes of nanoparticles. These three peaks are reproducible, not only in spectral positions, but also in the relative intensity ratios in each sample measured. The blueshifted peak at 415 nm for our nanoparticles of diameter 1.5 nm is also consistent with the value of energy estimated from the size-dependent spectra of Murray *et al.*[5]. The main component of our sample in toluene, therefore, is identified as only $(CdSe)_{33}$ and $(CdSe)_{34}$. The spectral profile of curve 1 is practically identical to those reported by Murray *et al.*[5] and Ptatschek *et al.*[6], who estimated the diameters of the nanoparticles to be 1.2 nm and 1.7 nm, respectively. These results show that these nanoparticles are especially stable, as they will grow under a wide range of preparation conditions.

Curve 2 of Fig. 2 shows the absorption spectrum of the solution prepared at 80 °C. A new broad peak appears at 480 nm, indicating that

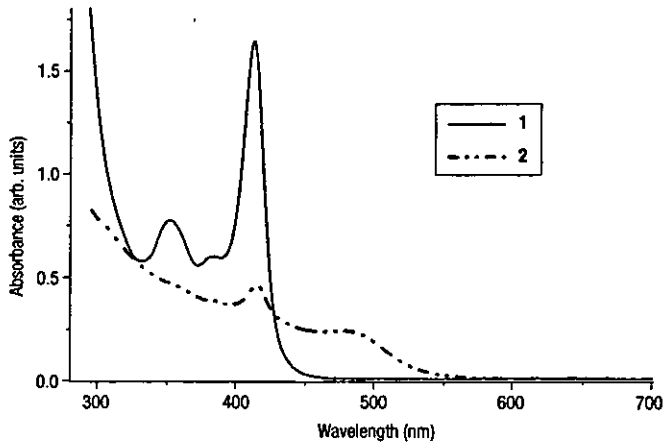

Figure 2 Optical absorption spectra at room temperature. Curve 1 is for CdSe nanoparticles prepared in toluene at 45 °C. Curve 2 is for a sample prepared at 80 °C, showing a new broad peak at 480 nm, with the sharp peak at 415 nm in curve 1 remaining without shift. At higher temperatures and longer times, the broad peak redshifts and its intensity increases, whereas the sharp peak decreases without shift.

particles of a new type begin to grow with a mean diameter of 2.0 nm and a distribution of ~10%, which is typical of small crystalline-like particles prepared with conventional colloid methods[5,6]. This broad peak shifts to longer wavelength with increasing temperature and time as the particle size increases. The sharp peak at 415 nm in curve 1 remains in curve 2 without shift, showing that $(CdSe)_{33}$ and $(CdSe)_{34}$ have particularly stable structures that are highly resistant against ripening even under conditions that favour the growth of larger particles.

Figure 3 shows X-ray diffraction profiles on our sample dried in air after removing the excess surfactant (curve 1), and on a powder sample of crystalline CdSe (curve 2). Curve 1 shows a series of five clear peaks indicated by arrows below $2\theta = 15°$. The first peak, at 2.80°, is the

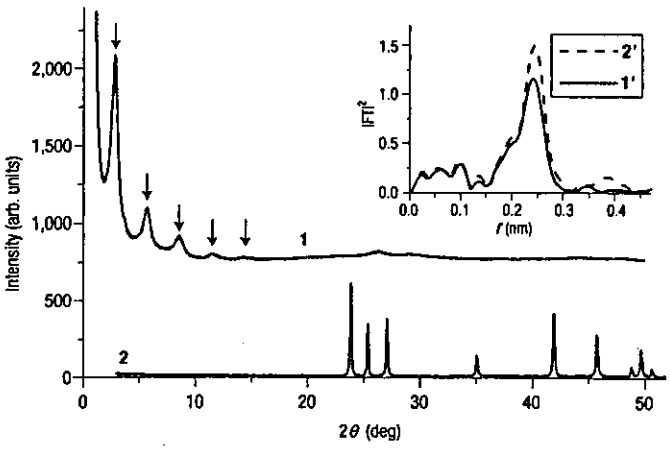

Figure 3 X-ray analysis of $(CdSe)_{33}$ and $(CdSe)_{34}$ structures. Curve 1 is the X-ray diffraction profile of a dried sample containing $(CdSe)_{33}$ and $(CdSe)_{34}$, taken with Cu-Kα radiation, and curve 2 is for a powder of bulk wurtzite CdSe. The curves 1′ and 2′ in the inset show the Fourier transform of EXAFS spectra at the Se-K edge of the nanoparticle and powder samples, respectively. *r*: nearest-neighbour distance.

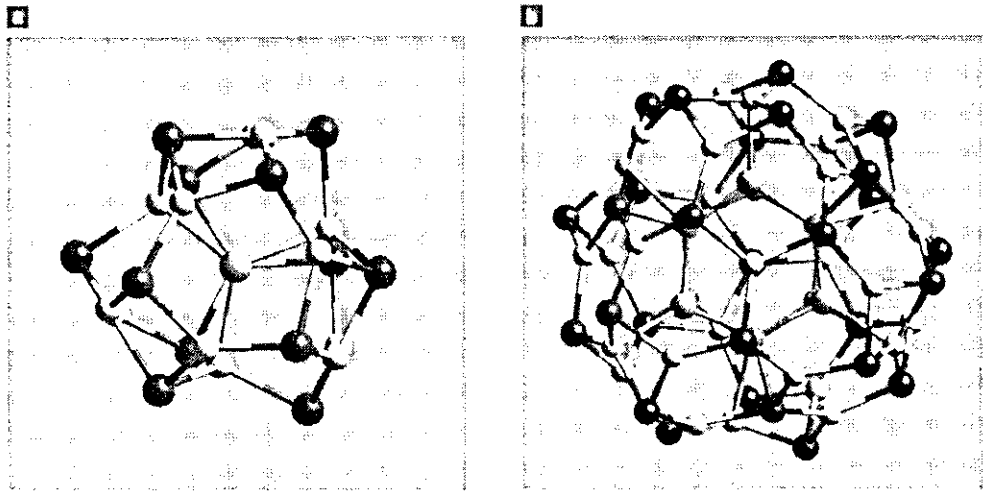

Figure 4 Structures of the $(CdSe)_n$ core–cage nanoparticles calculated to be most stable, viewed down a threefold symmetry axis. a, $(CdSe)_{13}$ has 3 four-membered and 10 six-membered rings on the cage of 12 Se (dark brown) and 13 Cd (white) ions with a Se (light brown) ion inside. **b**, $(CdSe)_{34}$ has a truncated-octahedral morphology formed by a $(CdSe)_{28}$-cage (Se, dark brown; Cd, white) with 6 four-membered and 8 × 3 six-membered rings. A $(CdSe)_6$ cluster (Se, light brown; Cd, green) encapsulated inside this cage provides additional network and stability.

fundamental reflection of the next four higher-order ones. These low-angle reflections show a self-assembled stack constructed from $(CdSe)_{33}$ and $(CdSe)_{34}$ with the surfactant acting as a spacer. Our wet chemical analysis and energy-dispersive X-ray (EDX) measurement of the solid sample show 1:1 stoichiometry of Cd/Se.

At angles of $2\theta > 20°$ there are only weak features in curve 1 where crystalline peaks of the bulk wurtzite CdSe would appear (curve 2). The width and shift of these weak features indicate that the range of structural ordering is ~1 nm in the arrays. EXAFS (extended X-ray absorption fine structure) measurement on $(CdSe)_{33}$ and $(CdSe)_{34}$ in toluene (Fig. 3, inset) shows a clear Fourier transform peak for a nearest-neighbour atom distance of 0.260 nm compared with 0.263 nm for bulk CdSe with tetrahedral bonding. The coordination number of Se ions is estimated to be 3.2 as compared with 4 in the bulk and 3 in the empty cage structure of, for example, C_{60} and $(BN)_n$. Peaks for further neighbours are weaker and much spread around the bulk second neighbour peak at 0.40 nm. These results show that our nanoparticles have basically three-dimensional sp^3-bonded Cd–Se with the modifications expected in particles of less than 100 atoms[9], consistent with our theoretical analysis given below.

First-principles calculations using ultrasoft pseudopotentials and the generalized gradient approximation[10] show $(CdSe)_n$ to be cage-like polyhedra with sp^3-like zigzag networks of alternately connected Cd and Se ions forming four- and six-membered rings similar to $(BN)_n$ (ref. 3) but highly puckered. Further stabilization occurs by filling the cage with a core connected to the cage. The choice of a highly symmetric cage with the right size of core imposes stringent restrictions for the stable nanoparticles if they are to retain a tetrahedral-like 3D network internally. This novel 3D core–cage structure shows magic behaviour (certain 'magic numbers' are strongly favoured) entirely different from fullerenes[1,2], BN-cages[3,4], shell structures of metallic clusters[8] and bulk fragments of compound nanoparticles[5–7]. The smallest polar cages with the highest possible symmetry (octahedral) are for $n = 12$, 16 and 28. Cages with $n = 12$ and 28 can accommodate, respectively, $(CdSe)_1$ and $(CdSe)_6$ inside as just the right sizes to form basically tetrahedral networks, making up stable $(CdSe)_{13}$ and $(CdSe)_{34}$ (Fig. 4) after rearranging their structures to maximize the binding energy. For $(CdSe)_{33}$, $(CdSe)_5$ fits well into the $(CdSe)_{28}$-cage, keeping a similar network. The encapsulation of $(CdSe)_3$ into an $n = 16$ cage is unfavourable as the inner space is too small. The optimal structure of $(CdSe)_{19}$ is a low-symmetry $n = 18$ cage encapsulating $(CdSe)_1$ with a local maximum in the binding energy leading to its weak magic nature (Fig. 1).

$(CdSe)_{13}$ has 12 Se and 13 Cd ions making up the puckered cage and a Se ion at the centre connected with four Cd ions 0.282 nm apart (Fig. 4a). The mean Cd–Se bond length is 0.264 nm. It is 0.614 eV lower in energy than an empty $n = 13$ cage, showing the preference for a 3D network. Fragments of bulk wurtzite and zinc blende[8] structures transform significantly on relaxation and lie a few electron volts higher

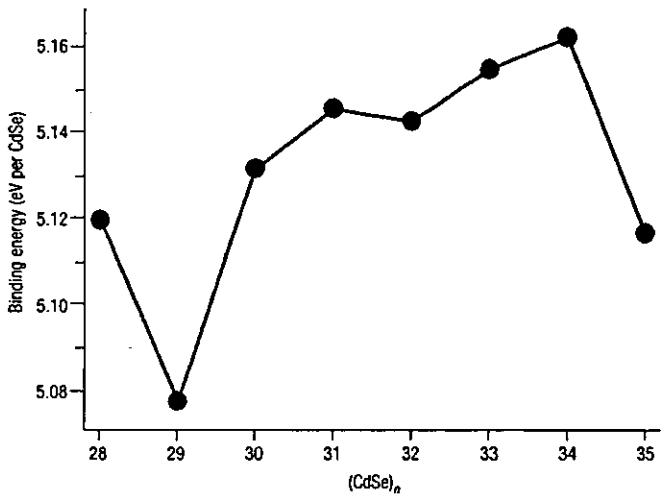

Figure 5 Calculated binding energies. The binding energies are calculated per CdSe molecule of $(CdSe)_n$ composed of a cage-like $(CdSe)_{28}$ with $(CdSe)_m$ inside ($n = 28 + m$, $m = 0, 1, \ldots, 7$).

in energy than the core–cage structures, ruling out the possibility that $(CdSe)_{13}$ and $(CdSe)_{34}$ have the bulk structure. The bond lengths in $(CdSe)_{34}$ (Fig. 4b) vary from 0.255 to 0.284 nm with the mean value of 0.266 nm, as compared with 0.268 nm calculated for the bulk. The mean nearest-neighbour coordination is 3.18. These results agree well with our EXAFS analysis. The largest diameter (1.45 nm) of $(CdSe)_{34}$ also agrees with our AFM estimate of 1.5 nm as well as the previous[5,6] estimates. The binding energy is maximum for $(CdSe)_{34}$ among $(CdSe)_{28+m}$ with $m = 0, 1, \ldots, 7$, as $(CdSe)_{m=6}$ is just the right size to fit inside a $(CdSe)_{28}$-cage, resulting in its extreme stability (Fig. 5). The binding energy decreases only slightly for $(CdSe)_{33}$ with $m = 5$. Our calculations also predict such nested cages with a core for other II–VI compounds, for example, ZnS and CdS, again supporting our experimental results. However, core–cage structures are less stable for III–V nanoparticles. For example, $(BN)_{13}$ with N at the centre is less stable than the empty $(BN)_{12}$ and $(BN)_{13}$-cages[3].

Our investigations demonstrate that $(CdSe)_n$ are extremely stable at some specific n, with novel core–cage structures predicted by theory. This sharply selective stability provides a definitive identification of stable compound nanoparticles of particular atomic numbers and compositions. Such 'magic clusters'[6] have long been sought or proposed on the basis of experiments. Our methods should allow their production in macroscopic quantities.

METHODS

PREPARATION

$(CdSe)_n$ nanoparticles were prepared in reverse micelles at a temperature of 45 °C under ambient pressure. Cadmium nitrilotriacetate, obtained by dissolving 0.16 g of $CdSO_4$ and 0.21 g of sodium nitrilotriacetic acid in 10 ml of water, was mixed with 1.2 ml of decylamine ($CH_3(CH_2)_9NH_2$) as surfactant. The cadmium ions bind to the amine groups of the surfactant. The solution is further mixed with 15 ml aqueous solution of sodium selenosulphate (Na_2SeSO_3) which dissociates in alkaline conditions to yield Se^{2-}. On adding toluene to this solution, the micelles move up into the toluene and transform into reverse micelles in which nanoparticles of CdSe form. Within a few minutes the toluene turns uniformly to greenish yellow, whereas the water remains colourless. The total reaction yield is more than 20%.

MASS SPECTROMETRY

The time-of-flight mass spectrometer used was a Bruker Daltonics, Reflex III, equipped with a nitrogen laser.

Received 8 July 2003; acccepted 10 December 2003; published 25 January 2004.

References

1. Kraetschmer, W., Lamb, L. D., Fostiropoulos, K. & Huffman, D. R. Solid C_{60}: A new form of carbon. *Nature* 347, 27–30 (1990).
2. Kumar, V. & Kawazoe, Y. Metal-encapsulated fullerene like and cubic caged clusters of silicon. *Phys. Rev. Lett.* 87, 045503 (2001).
3. Seifert, G., Fowler, P. W., Mitchell, D., Porezag, D. & Frauenheim, Th. Boron-nitrogen analogues of the fullerenes: Electronic and structural properties. *Chem. Phys. Lett.* 268, 352–358 (1997).
4. Stephan, O. *et al.* Formation of small single-layer and nested BN cages under electron irradiation of nanotubes and bulk material. *Appl. Phys. A* 67, 107–111 (1998).
5. Murray, C. B., Norris, D. J. & Bawendi, M. G. Synthesis and characterization of nearly monodisperse CdE (E = S, Se, Te) semiconductor nanocrystallites. *J. Am. Chem. Soc.* 115, 8706–8715 (1993).
6. Ptatschek V. *et al.* Quantized aggregation phenomena in II–VI semiconductor colloids. *Ber. Bunsenges. Phys. Chem.* 102, 85–95 (1998).
7. Peng, X. *et al.* Shape control of CdSe nanocrystals. *Nature* 404, 59–61 (2000).
8. Martin, T. P. Shells of atoms. *Phys. Rep.* 273, 199–241 (1996).
9. Pinto, A. *et al.* Evidence for truncated octahedral clusters in supported gold clusters. *Phys. Rev. B* 51, 5315–5321 (1995).
10. Kresse, G. & Furthmuller, J. Efficient iterative schemes for ab-initio total energy calculations using a plane-wave basis set. *Phys. Rev. B* 55, 11169–11186 (1996).

Acknowledgements

The authors are indebted to M.Tachiki, Y.Nishina, K.Suzuki, A.Inoue, K.Sumiyama, T.Ohsuna and J. R. Anderson for discussions and comments.
Correspondence and requests for materials should be addressed to A.K.
Supplementary Information accompanies the paper on www.nature.com/naturematerials

Competing financial interests

The authors declare that they have no competing financial interests.

Available online at www.sciencedirect.com
SCIENCE DIRECT
ELSEVIER
Applied Surface Science 242 (2005) 281–286
applied surface science
www.elsevier.com/locate/apsusc

Preparation of silica encapsulated CdSe quantum dots in aqueous solution with the improved optical properties

Xingping Zhou[a,*], Yoshio Kobayashi[b], Volodya Romanyuk[a], Noriaki Ochuchi[c], Motohiro Takeda[c], Shin Tsunekawa[d], Atsuo Kasuya[a]

[a]*Center for Interdisciplinary Research, Tohoku University, Aramaki aza Aoba, Sendai 980-8578, Japan*
[b]*Department of Chemical Engineering, Graduate School of Engineering Tohoku University, Sendai 980-8579, Japan*
[c]*Graduate School of Medicine, Tohoku University, Sendai 980-8574, Japan*
[d]*Institute for Materials Research, Tohoku University, Sendai 980-8577, Japan*

Accepted 20 August 2004
Available online 12 October 2004

Abstract

Silica encapsulated CdSe quantum dots (QDs) have been prepared by the use of 3-mercaptopropyl trimethoxysilane (MPS) in a weak alkaline solution in ambient atmosphere at room temperature. The average size of the multicore-shell structured CdSe/SiO_2 is 28.0 nm and that of the CdSe QDs is 3.4 nm from the observation of the transmission electron micrographs (TEMs). The enhanced photoluminescence (PL) intensity of the QDs has been observed by passivation of silica shell. The increased photochemical and -physical stability of the encapsulated CdSe/SiO_2 QDs has also been demonstrated.

PACS: 8.20.n; 72.80.Tm; 74.25.Gz

Keywords: Encapsulation; CdSe; Quantum dots; SiO_2; Passivation; Photoluminescence (PL); Stability

1. Introduction

In recent years, interests have been greatly increased in the scientific and technological aspects of semiconductor quantum dots (QDs). Due to small size, such zero-dimensional structures demonstrate unique chemical and physical properties which are different from those of bulk solids [1,2]. That the number of atoms on the surface becomes comparable or even higher than inside leads to the changes in the electronic structure, state density and optical properties as consequence. However, semiconductor becomes chemically active especially while the size decreases to the quantum size range (several nanometers). Therefore, the specific physical and chemical properties are eliminated and the application is greatly limited. A way to remove the influence is a process named as passivation, which consists of

* Corresponding author. Tel.: +81 22 217 5758; fax: +81 22 217 5756.
E-mail address: zhou@cir.tohoku.ac.jp (X. Zhou).

0169-4332/$ – see front matter © 2004 Elsevier B.V. All rights reserved.
doi:10.1016/j.apsusc.2004.08.022

surface atoms bonding to a different material with inert chemical properties. W.L. Wilson and P. Mulvaney et al. have concluded that silica is a quite suitable material to be a coating or encapsulating inert substance [3,4]. It has been successfully applied in passivation of Au [5], Ag [6], and CdS particles [7].

Owing to the potential and practical possibility of cadmium selenide (CdSe) with a suitable band gap (1.76 eV), for applications in industrial and medical fields, currently, the preparation, absorption, and exciton luminescence processes in CdSe nanoparticles have been extensively studied [8–11]. In particular, CdSe semiconductor quantum dots have greatly interested biologists and pharmaceutical scientists [12,13]. By now, quantum dot quantum wall (QDQW) nanocrystals heterostructurally coated with materials with higher band gap of CdS [14,15], ZnS [16], and even multilayers of HgSe/CdSe have been successfully fabricated and their physical and chemical properties have been apparently improved [17]. Moreover, CdSe nanoparticles have been encapsulated with silica as a film and their electronic properties can be improved obviously [18–21]. However, there is no any report on the preparation of core-shell structured CdSe/SiO_2 quantum dots (QDs) except the work reported by Rogach et al. [22] in which the PL intensity of CdSe Qds dramatically decreased after the passivation of SiO_2 in relatively complicated conditions.

In this work a citrate-stabilized aqueous suspension of quantum sized CdSe nanoparticles was prepared at room temperature based on a simple chemical precipitation in quite mild conditions. Also, these QDs were successfully encapsulated with silica by a slow deposition of silica solute from a silicate solution while being transferred into ethanol. Moreover, the valid passivation was confirmed with the absorbance and the photoluminescence of the CdSe particles was promoted after being coated with SiO_2. Meantime, the possible mechanisms for the passivation and the promotion were simply discussed.

2. Experimental

2.1. Materials

Special grade reagents (Wako Pure Chemical Ind.) of sodium silicate solution ($Na_2O(SiO_2)_{2.0-2.31}$, 52.0–57.0%), 3-mercaptopropyl trimethoxysilane (MPS), cadmium sulfate ($CdSO_4 \cdot 8/3H_2O$, >99%), selenium powder (Se, >99%), sodium nitrilotriacetate (Na_3-NTA:$N(CH_2COONa)_3$), sodium sulfite, ethanol, and sodium citrate were used as received. Water was double-distilled and deionized to have an electrical resistance higher than 18 MΩ cm^{-1}.

2.2. Preparation of the stable suspension of CdSe quantum dots

Firstly, 1.0 ml of 0.15 M $CdSO_4$ was mixed with Na_3NTA at a mole ratio of $[Cd^{2+}]:[NTA^{3-}] = 5:4$ to form a Cd–NTA complex. Then, 1 ml of 1.6 wt.% Na-citrate was added to the solution of the Cd–NTA complex. Finally, 0.75 ml of aqueous solution of 0.2 M sodium selenosulfate (Na_2SSeO_3) with excess Na_2SO_3 that was prepared by stirring 0.79 g of Se powder in 50 ml of 0.5 M Na_2SO_3 at 70 °C for 24 h were added to the above solution to form a solution of 0.006 M cadmium ion and then aged it at room temperature for 5 days. The reaction equation is shown as the following:

$$Cd^2 + 2OH^- + SeSO_3^{2-} \rightarrow CdSe + SO_4^{2-} + H_2O$$

2.3. Preparation of silica encapsulated CdSe nanoparticles

The established standard conditions for preparation of silica encapsulated CdSe QDs were shown as following.

Two milliliter of the formed CdSe stable suspension was diluted with 17 ml water and treated ultrasonically for 30 min. Then, 0.2 ml of freshly prepared 0.02 wt.% MPS and 0.8 ml of 0.54% sodium silicate solution at pH 10.5 were added to the above suspension and then aged at room temperature for 5 days with vigorous magnetic stirring. Hence, the silica slowly polymerizes onto the MPS-modified CdSe QDs. Finally, the resulting dispersion was transferred to ethanol at a volume ratio of 1:5, and then the excessive dissolved silicate precipitates out mainly on the existing cores, which leads to an increase in the thickness of the silica shell.

2.4. Electron microscopy

The products were observed with a JEM-2000EX II transmission electron microscope (TEM) with an

acceleration voltage of 200 kV and an EDMAX scanning electron microscope (SEM). Also, atomical composition of the products was analyzed with energy dispersive X-ray (EDX) measurements equipped with the SEM.

2.5. Optical measurements

UV spectrometry of CdSe nanoparticles in suspension before and after coating silica was conducted with an UV–vis spectrophotometer, Hitachi U-2000, where the light path length was 1 cm. In addition, the photoluminescence of these particles was investigated with a JASCO FP-750 Spectrofluorometer.

3. Results and discussion

3.1. Formation of CdSe quantum dots without and with silica encapsulating

After mixing Cd–NTA complex with Na_2SeSO_3 solution and aging it at room temperature for 5 days, a very stable deep red suspension was formed. This suspension was stable kinetically at least for 1 year. Since citrate ions act as protect agents for a variety of inorganic colloids including CdS particles [7], probably the citrate ions also seemed to be of the same function for the current system. This was confirmed simply with the fact that the suspension was fairly unstable in the absence of Na-citrate.

Fig. 1a shows transmission electron micrograph of the solid product from the stable suspension. Obviously uniform aggregates of CdSe particles with an average size of 22.5 nm were observed together with several tens of primary particles. The wet chemical analysis measurement of the solid sample showed 1:1 stoichiometry of Cd:Se. From powder XRD measurements on dried nanoparticles, the nanoparticles were in CdSe cubic structure which is typical for low temperature prepared CdSe particles.

Fig. 1b shows transmission electron micrograph of the silica encapsulated CdSe QDs. It obviously revealed that plural QDs were encapsulated completely with silica matrix. The average sizes of the microcapsules and the QDs were 28.0 and 3.4 nm, respectively. It should be noted that no aggregates were observed in the encapsulated particles. Thus, improvement of the particle dispersity was achieved by encapsulation.

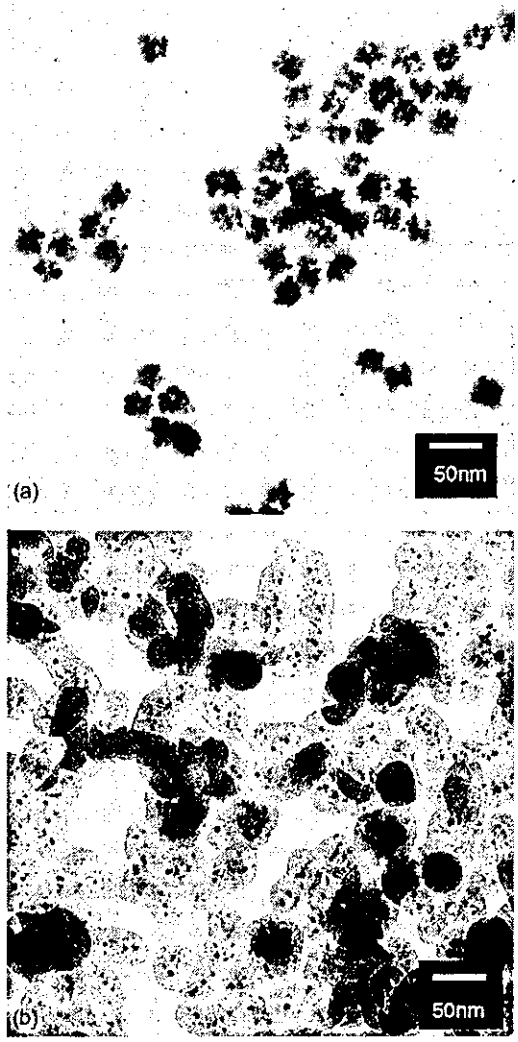

Fig. 1. Transmission electron micrographs of CdSe nanoparticles before (a) and after silica encapsulating (b).

It is hardly possible for silica to deposit directly on the surface of CdSe nanoparticles because of low affinity between them. MPS is a bifunctional coupling agent to bind with Cd atom on the surface in its mercapto group as well as a silane coupling agent. It has been successfully applied to the formation of silica coated CdS particles [7]. The adhesion of silicate